Article:
Vellios, N., Keating, P. and Tsakiropoulos, P. (2021) On the Microstructure and Properties of the Nb-23Ti-5Si-5Al-5Hf-5V-2Cr-2Sn (at.%) Silicide-Based Alloy—RM(Nb)IC. Metals, 11 (11). 1868. ISSN: 2075-4701

https://doi.org/10.3390/met11111868

metals

MDPI

Article

On the Microstructure and Properties of the Nb-23Ti-5Si-5Al-5Hf-5V-2Cr-2Sn (at.%) Silicide-Based Alloy—RM(Nb)IC

Nikos Vellios, Paul Keating and Panos Tsakiropoulos *

Department of Materials Science and Engineering, Sir Robert Hadfield Building, The University of Sheffield, Mappin Street, Sheffield S1 3JD, UK; n.vellios@gmail.com (N.V.); Paul_keating85@hotmail.com (P.K.)
* Correspondence: p.tsakiropoulos@sheffield.ac.uk

Abstract: The microstructure, isothermal oxidation, and hardness of the Nb-23Ti-5Si-5Al-5Hf-5V-2Cr-2Sn alloy and the hardness and Young's moduli of elasticity of its Nb_{ss} and Nb_5Si_3 were studied. The alloy was selected using the niobium intermetallic composite elaboration (NICE) alloy design methodology. There was macrosegregation of Ti and Si in the cast alloy. The Nb_{ss}, αNb_5Si_3, γNb_5Si_3, and HfO_2 phases were present in the as-cast or heat-treated alloy plus TiN in the near-the-surface areas of the latter. The vol.% of Nb_{ss} was about 80%. There were Ti- and Ti-and-Hf-rich areas in the solid solution and the 5-3 silicide, respectively, and there was a lamellar microstructure of these two phases. The V partitioned to the Nb_{ss}, where the solubilities of Al, Cr, Hf, and V increased with increasing Ti concentration. At 700, 800, and 900 °C, the alloy did not suffer from catastrophic pest oxidation; it followed parabolic oxidation kinetics in the former two temperatures and linear oxidation kinetics in the latter, where its mass change was the lowest compared with other Sn-containing alloys. An Sn-rich layer formed in the interface between the scale and the substrate, which consisted of the Nb_3Sn and Nb_6Sn_5 compounds at 900 °C. The latter compound was not contaminated with oxygen. Both the Nb_{ss} and Nb_5Si_3 were contaminated with oxygen, with the former contaminated more severely than the latter. The bulk of the alloy was also contaminated with oxygen. The alloying of the Nb_{ss} with Sn increased its elastic modulus compared with Sn-free solid solutions. The hardness of the alloy, its Nb_{ss}, and its specific room temperature strength compared favourably with many refractory metal-complex-concentrated alloys (RCCAs). The agreement of the predictions of NICE with the experimental results was satisfactory.

Keywords: refractory metal intermetallic composites; Nb silicide-based alloys; high-entropy alloys; complex concentrated alloys; alloy design; oxidation; hardness; Young's modulus

Citation: Vellios, N.; Keating, P.; Tsakiropoulos, P. On the Microstructure and Properties of the Nb-23Ti-5Si-5Al-5Hf-5V-2Cr-2Sn (at.%) Silicide-Based Alloy—RM(Nb)IC. *Metals* **2021**, *11*, 1868. https://doi.org/10.3390/met11111868

Academic Editor: Martin Heilmaier

Received: 25 October 2021
Accepted: 16 November 2021
Published: 20 November 2021

1. Introduction

Interest in RM(Nb)ICs, i.e., refractory metal (RM) intermetallic composites based on Nb, also known as Nb-silicide-based alloys or Nb in situ composites, as potential metallic ultra-high temperature materials (UHTM) to replace Ni-based superalloys in high-temperature structural applications in aero engines, has arisen from early research on binary Nb-Si alloys and experimental data that showed that such RMICs could offer an attractive combination of high temperature strength, creep resistance, and room temperature fracture toughness (e.g., see [1]). Another contributing factor was the phase equilibria of the binary system [2] that makes it possible to cast in situ composites consisting of a RM terminal solid solution, namely, the bcc Nb solid solution (Nb_{ss}), and the creep-resistant tetragonal Nb_5Si_3 silicide. The latter can have the high-temperature βNb_5Si_3 (tI32, $D8_m$, prototype W_5Si_3) or the low-temperature αNb_5Si_3 (tI32, $D8_l$, prototype Cr_5B_3) structure that are isomorphous but with distinctly different lattice parameters α and c [2].

The early research focused on alloys of the Nb-Si-Ti-Hf-Cr-Al system, a typical example of which is the MASC alloy Nb-25Ti-16Si-8Hf-2Al-2Cr (at.%) [3]. The initial research

showed (a) that the Si concentration should be in the range 16 < Si < 22 at.% in order to meet the creep property goal and (b) that the alloying with Al, Cr, Ti, and Hf plus RM and other simple metal and metalloid element additions could enable the alloy developer to achieve a balance of strength, creep, and toughness with improved oxidation resistance [4,5]. Even with RM alloying additions, e.g., Mo, it is possible to have RM(Nb)ICs with densities as low as 6.55 g/cm^3 [6] compared with the typical densities of about 9 g/cm^3 for Ni-based superalloys.

Vanadium gives strong solid solution strengthening to Nb [7]. The addition of V in Si-free Nb-Ti-Cr-Al-based alloys improved their room temperature ductility and tensile and rupture strength above 1000 °C [8,9]. Vanadium is also a solid solution strengthening element in RM(Nb)ICs [7] and destabilises the stable (tP32) Nb_3Si silicide in favour of the Nb_5Si_3 silicide but has an adverse effect on the oxidation of Nb [7]. Control of pest oxidation in the temperature range 700 °C to 900 °C ("pest regime"), which is an essential requirement for RM(Nb)ICs and other metallic UHTMs, for example, refractory high-entropy alloys (RHEAs) and refractory complex concentrated alloys (RCCAs) [10,11], has been demonstrated to be possible with the addition of Sn [3,12], but the "desirable" Sn content is undecided [13–16]. Control of the contamination by interstitials of the aforementioned metallic UHTMs is also essential [10,17].

It is recognised that the oxidation of RM(Nb)ICs at intermediate (≤900 °C) and high temperatures (≥1200 °C) is controlled by the oxidation of the Nb_{ss} and can be very sensitive to the volume fraction of the latter [3,6,18,19], which depends not only on the Si content of the RM(Nb)IC but also on the other alloying additions [14,15,20–23]. Could an RM(Nb)IC with high vol.% Nb_{ss} have an acceptable oxidation behaviour, meaning a low mass change in isothermal oxidation, and be resistant to pesting in the pest oxidation regime? What would be the contamination by oxygen of such an alloy? One motivation for the research presented in this study was to answer these questions. (The answer to the question about contamination is very important owing to the sensitivity of RM(Nb)ICs, RHEAs, and RCCAs to contamination by interstitials and the effect of the latter on properties [10].)

The mechanical behaviour of RM(Nb)ICs at in-service temperatures depends on their microstructural stability. Of particular interest is the stability (a) of tetragonal (tI32) Nb_5Si_3 [3,8] compared with hexagonal (hP16) γNb_5Si_3, which is isomorphous with Hf_5Si_3 and Ti_5Si_3 [24]; (b) of the Nb_{ss}; and (c) of eutectic microstructure(s). RM additions can stabilise eutectic microstructures after exposure to high temperatures (e.g., 1500 °C/100 h), for example, the addition of Mo, Ta, or W in the RM(Nb)ICs YG4 [25], YG5, YG6, YG8 [26], and CM1 [27], as well as Hf in synergy with Sn in the Ti-free alloy EZ1 [28] (for nominal composition of alloys, see the Table 1 in the Appendix A). The stability of the Nb_{ss} can be affected by the synergy of Al with Sn in the absence/presence of Hf (see the Ti-free alloys EZ4 and EZ7 in [28]) or the synergy of Hf with Al, Sn, and Ti in Nb-24Ti-18Si-5Al-5Hf-5Sn (alloy EZ5 in [29]). The stability of hexagonal Ti_5Si_3 in RM(Nb)ICs should be avoided because this silicide is detrimental for the creep of RM(Nb)ICs [8,30]. However, in the microstructure of RM(Nb)ICs with high Ti and Hf concentrations, which are expected to improve their oxidation, the hexagonal Nb_5Si_3 can be stable instead of or with the tetragonal Nb_5Si_3. Furthermore, in the Nb-Hf-Si system, the Hf_5Si_3 can be stable to lower temperatures (in other words, Nb stabilises the hP16 Hf5Si3 to lower temperatures) [31,32]. Accordingly, after exposure to high temperature, the stability or not of Nb_{ss} and hexagonal Nb_5Si_3 in RM(Nb)ICs, where the transition metals (TMs) Cr, Hf, and Ti are in synergy with another (than Nb) RM and with the simple metal and metalloid element additions Al, Si, and Sn, is critical because of the knock-on effect these phases can have on the creep and oxidation performance in-service. What type of Nb_5Si_3 (meaning α, β or γ) can be stable in RM(Nb)ICs with high vol.% Nb_{ss}? Another motivation for the research presented in this study was to answer this question.

The structure of the article is as follows. A brief description of the alloy selection is given before the experimental details. The results for the microstructure of the alloy in the as-cast and heat-treated conditions are presented in advance of the oxidation, hardness,

and nano-indentation results. The discussion considers first the microstructure of the alloy and then the oxidation and hardness of the alloy, and the hardness and elastic moduli of the solid solution and 5-3 silicide are discussed. Finally, the experimental results are compared with the calculations (predictions) of the alloy design methodology NICE [17].

2. Alloy Design/Selection

The alloy design methodology NICE was used to select the alloy for this research, as described in [10,11,17]. The property goal was that the mass change per unit area ($\Delta W/A$) for isothermal oxidation in air at 800 °C should not exceed 20 mg/cm^2. The alloy design constraints were as follows: (i) the RM(Nb)IC should be from the Nb-Si-Ti-Hf-Cr-Al system with the addition of Sn and V; (ii) the stable phases in its microstructure should be the Nb_{ss} and Nb_5Si_3; (iii) the vol.% Nb_{ss} should not be less than 70%; (iv) the room temperature yield strength (σ_y) should not be less than 1300 MPa (or 400 HV); and (v) the macrosegregation of Si (MACSi) should not be higher than 4 at.%. The Si, Sn, and V additions (constraint (i)) that have opposite effects on oxidation were chosen to study whether an alloy with a high vol.% Nb_{ss} and V addition cannot suffer from pest oxidation.

The nominal composition of the selected alloy was Nb-22.8Ti-5.1Si-4.8Al-4.9Hf-4.8V-2.1Cr-2.2Sn or (rounded to the nearest whole number) Nb-23Ti-5Si-5Al-5Hf-5V-2Cr-2Sn (at.%). According to NICE, the stable phases in this alloy should be the Nb_{ss} and Nb_5Si_3, and the alloy should have 75.5 vol.% Nb_{ss}, $\Delta W/A$ = 14.8 mg/cm^2, MACSi = 3.7 at.% and σ_y = 1481 MPa. The former three values were the averages of the values calculated from the relationships in NICE that correlate vol.% Nb_{ss}, $\Delta W/A$, and MACSi with the parameters δ, $\Delta\chi$, and VEC, and the yield stress was the average of the values that link Vickers hardness with the parameters VEC, ΔS_{mix}, and $\Delta\chi$ in NICE.

3. Experimental

High-purity (wt.%) elements (Nb 99.99%, Al 99.999%, Si 99.999%, Ti 99.99%, Cr 99.99%, Sn 99.99%, V 99.7%, and Hf 99.8%) were used as the starting materials to make button/ingots of 300 g weight of the alloy in an argon atmosphere using arc melting with a non-consumable tungsten electrode and a water-cooled copper crucible. In order to improve homogeneity, melting was repeated five times by turning over the button/ingot after each melt. The ingots were cooled down to ambient temperature inside the arc melting furnace. Cubic specimens that were cut from the bulk of the ingot were wrapped in Ta foil, placed in an alumina boat, and were heat treated at 1500 °C in a tube furnace for 100 h under a Ti-gettered argon atmosphere. The heat treatment temperature was decided following study of small-sized samples (results not shown) using differential scanning calorimetry (Stanton Redcroft STA-1500 DSC/DTA, Thermal Scientific plc., Odessa, TX, USA) to ensure avoidance of liquation during heat treatment. The DSC specimens were also cut from the bulk of the button/ingot.

Standard metallographic preparation was used to prepare specimens for study by X-ray diffraction (XRD) and electron beam microprobe analysis (EPMA). A Philips X-ray diffractometer with monochromatic Cu Kα (λ = 1.5418) radiation was used for the identification of the phases, which was done using JCPDS data. Secondary electron (SE) and backscatter electron (BSE) imaging and quantitative chemical analyses were performed using a JEOL 8600 electron probe micro-analyser (JEOL, Tokyo, Japan). High purity elements and Hf_2Si [33], Al_2O_3, and BN, which had been polished to a 1 μm finish, were used for standardisation purposes. Analysis was performed at 15 kV, 20 nA, and about a 1 μm diameter beam, and, at each measurement, the probe diameter was adjusted so as to achieve a dead time less than 20%. At least ten analyses were done for each phase in different parts (top, bulk, and bottom) of the button/ingot. Average concentrations and the minimum and maximum concentrations of at least ten analyses of an element in a phase or region of the ingot are given in the tables in this article. Measurements of the area fraction of Nb_{ss} were performed using software available on the microprobe, and the contrast of the phases was adjusted under BSE imaging. Area fractions were measured for the same

areas that were used for large area analyses in EPMA. At least ten measurements were taken for each alloy, all at the same magnification (X350).

Thermogravimetric analysis (TGA) of the alloy was carried out using a Stanton Redcroft thermo-balance (Thermal Scientific plc., Odessa, TX, USA) equipped with an alumina tube furnace. Small cube-shaped specimens ($5 \times 5 \times 5$ mm^3) were cut from the as-cast ingot. Each specimen was placed in a small cylindrical alumina crucible, which was then placed on the thermo-balance. The tube furnace was preheated to the selected temperature. The bottom of the crucible was in direct contact with a thermocouple. The isothermal oxidation of the alloy was evaluated at 700, 800, and 900 °C for up to 100 h. The oxides that formed on the surface of the specimens and spalled off were ground to powder and studied using XRD. EPMA was performed on cross sections of oxidised specimens.

The Vickers hardness of the alloy in the as-cast and heat-treated conditions was measured with a load of 10 kg. At least ten measurements were taken. The density of the alloys was measured using the Archimedes' principle and a Sartorious LA2305 electronic precision balance (Sartorius Lab Instruments GmbH & Co. KG, Göttingen, Germany), equipped with a density determination kit. The average and minimum and maximum values of the hardness and density of the alloys are given in this article.

The as-cast and heat-treated microstructures made it possible to measure the hardness and elastic moduli of Nb_{ss} and Nb_5Si_3 using nano-indentation. For this work, we used a Hysitron Inc. TriboScope ® Nanomechanical Testing System (Hysitron Inc., Minneapolis, MN, USA) equipped with the software package TriboScope version 3.5L and a TriboIndenter that was fitted with a Berkovich style tip, which is a flat three-sided, diamond-tipped pyramid with a total induced angle of 142.3° and a half angle of 65.35° [34]. The radius of curvature of the tip was 150 nm. This signified that only a low level of detail could be achieved during imaging compared with a sharper tip, owing to imaging using an atomic force microscope (AFM) that was linked to the nano-indenter. A load of 7000 μN was used for the nano-indentation measurements.

4. Results

4.1. As-Cast (NV1-AC)

The actual chemical composition of NV1-AC was 51.4Nb-23Ti-6.2Si-5Al-2.1Cr-5.4Hf-2.2Sn-4.7V. This was the average composition of all the analyses taken from the bottom, bulk, and top areas of the as-cast button/ingot. The density of the alloy was 7.38 g/cm^3 (Table 1). The microstructure in all parts of the ingot consisted of Nb_{ss}, Nb_5Si_3, HfO_2, and Nb_{ss} + Nb_5Si_3 fine-scale lamellar microstructure (Figures 1–3). The latter was "connected" with Nb_5Si_3 that had Nb/(Ti + Hf) less than one and an average <Si> of about 39 at.% (Figure 3) but not with Nb_5Si_3 with Nb/(Ti + Hf) greater than one and an average <Si> of about 37 at.% (Figure 2b) (<Si> = Al + Si + Sn). The XRD indicated the possible presence of Nb_3Si. However, exhaustive study using EPMA to find Nb_3Si, the presence or absence of which is important to understand how the lamellar microstructure formed (see discussion), did not confirm the existence of Nb_3Si in NV1-AC.

Table 1. Density, Vickers hardness, and vol.% of Nb_{ss} and Nb_5Si_3. (Average values are shown in bold numbers).

Alloy	*Density (g/cm^3)*	*Hardness (HV)*	*Vol.% Nb_{ss}*	*Vol.% Nb_5Si_3*
NV1–AC	7.26–7.43	454–503	78.5–81.6	16.1–19.8
	7.38 ± 0.1	**475** ± 17	**79.6** ± 1.1	**18.0** ± 1.4
NV1–HT	-	376–488	79.2–83.6	15.7–18.1
	-	**454** ± 35	**81. 0** ± 1.5	**16.9** ± 0.9

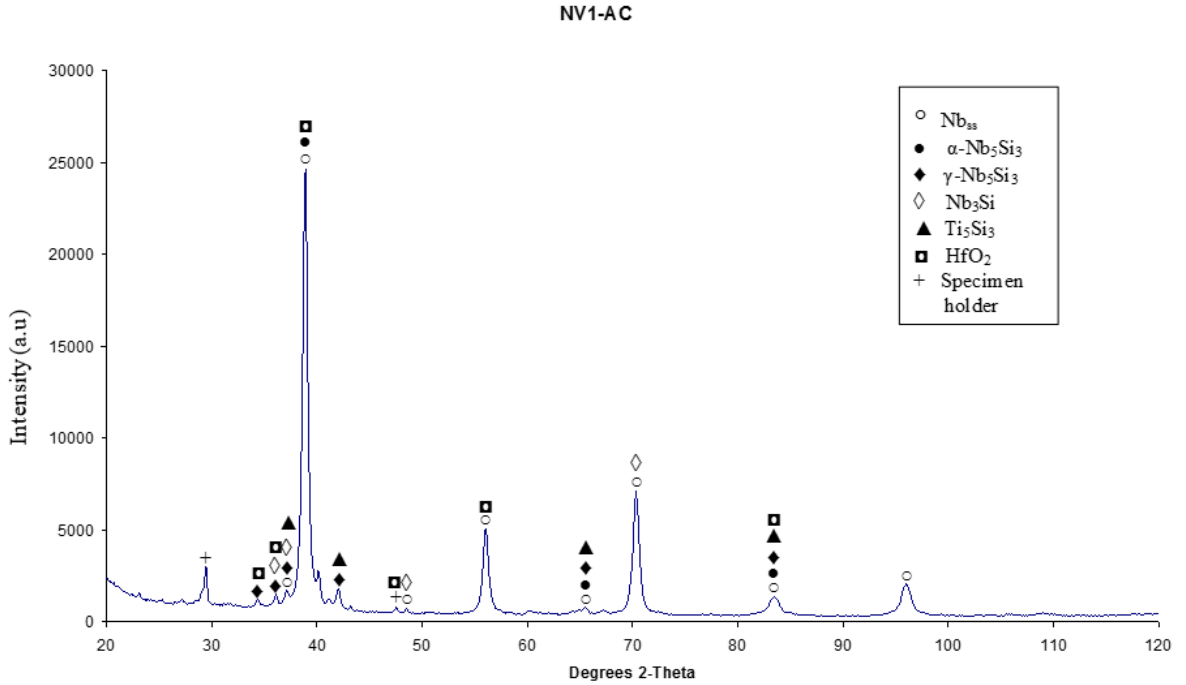

(**a**)

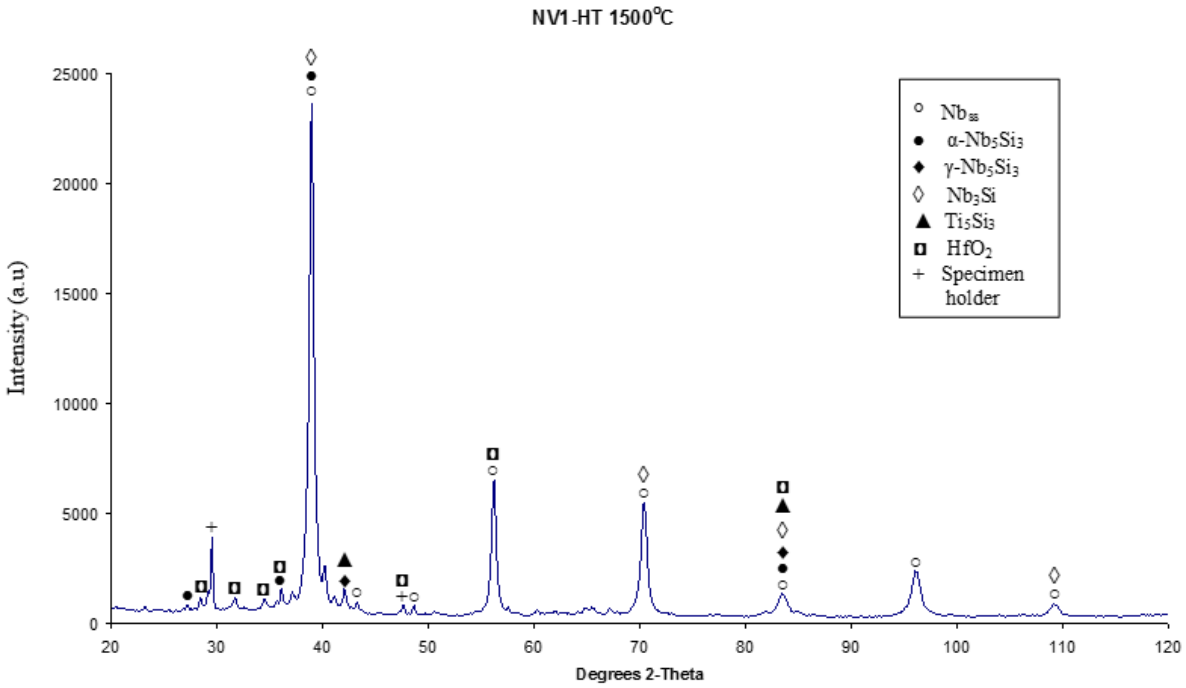

(**b**)

Figure 1. X-ray diffractograms of the alloy NV1 (**a**) as cast and (**b**) heat treated.

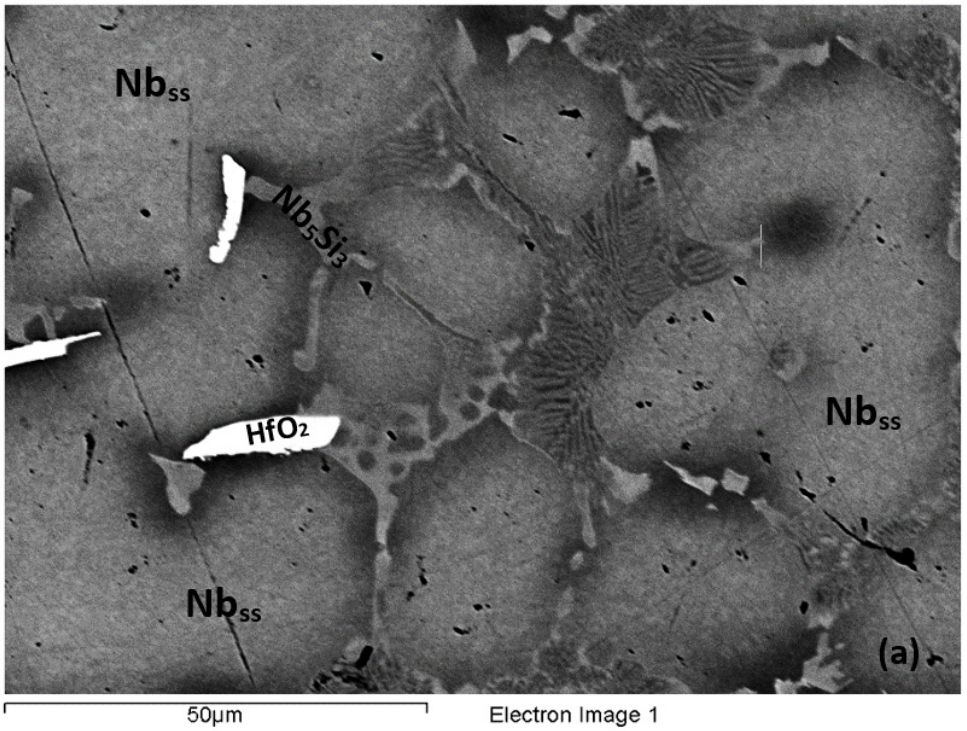

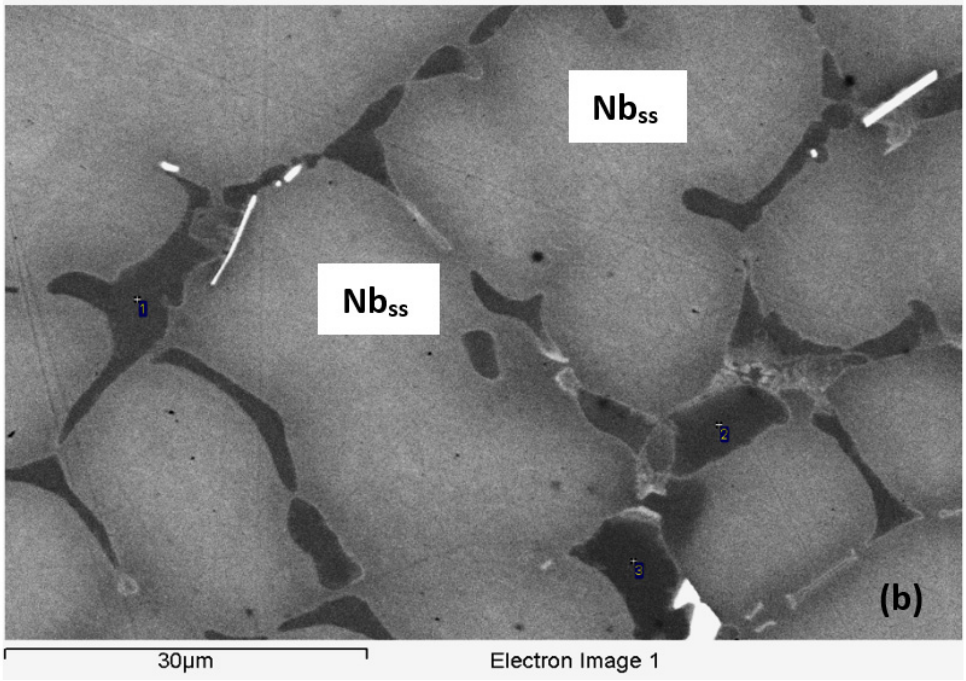

Figure 2. *Cont*.

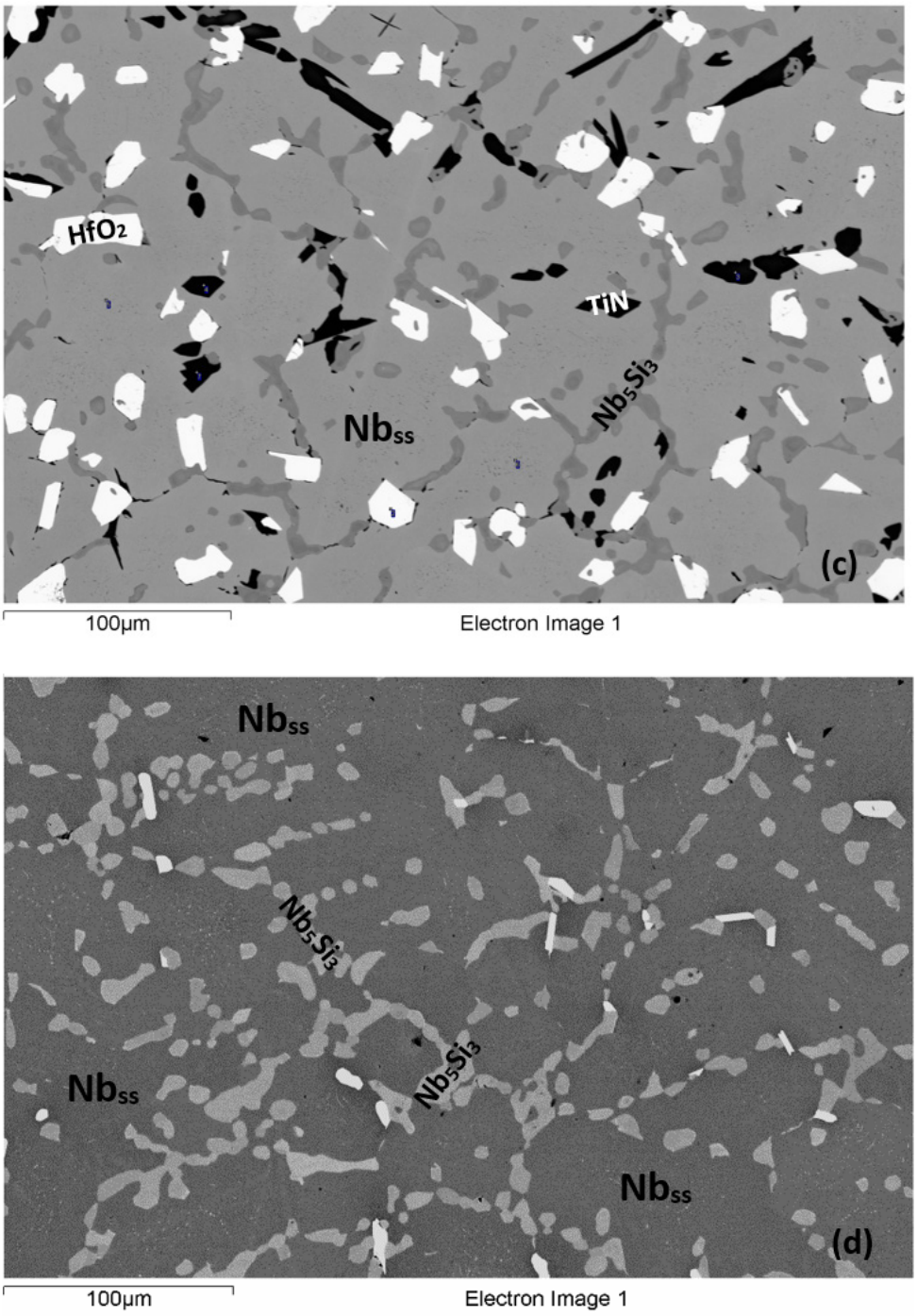

Figure 2. BSE images of the microstructure of NV1. (**a**) and (**b**) as cast; (**c**) and (**d**) heat treated. (**a**) top and (**b**) bulk of NV1-AC, (**c**) near surface area of NV1-HT, and (**d**) bulk of NV1-HT. Analysis in (**b**) as follows. 1: 5-3 silicide 35.9Nb-18.8Ti-32.1Si-4.1Al-1Cr-6Hf-0.9Sn-1.2V, Nb/(Ti + Hf) = 1.45, <Si> = 37.1 at.%, 2: 5-3 silicide 33.7Nb-19.4Ti-33.1Si-3.9Al-0.6Cr-6.5Hf-0.8Sn-2V, Nb/(Ti + Hf) = 1.30, <Si> = 37.8 at.%, 3: 5-3 silicide 33.8Nb-20.8Ti-31.9Si-3.8Al-0Cr-7Hf-0.9Sn-1.8V, Nb/(Ti + Hf) = 1.22, <Si> = 36.6 at.%.

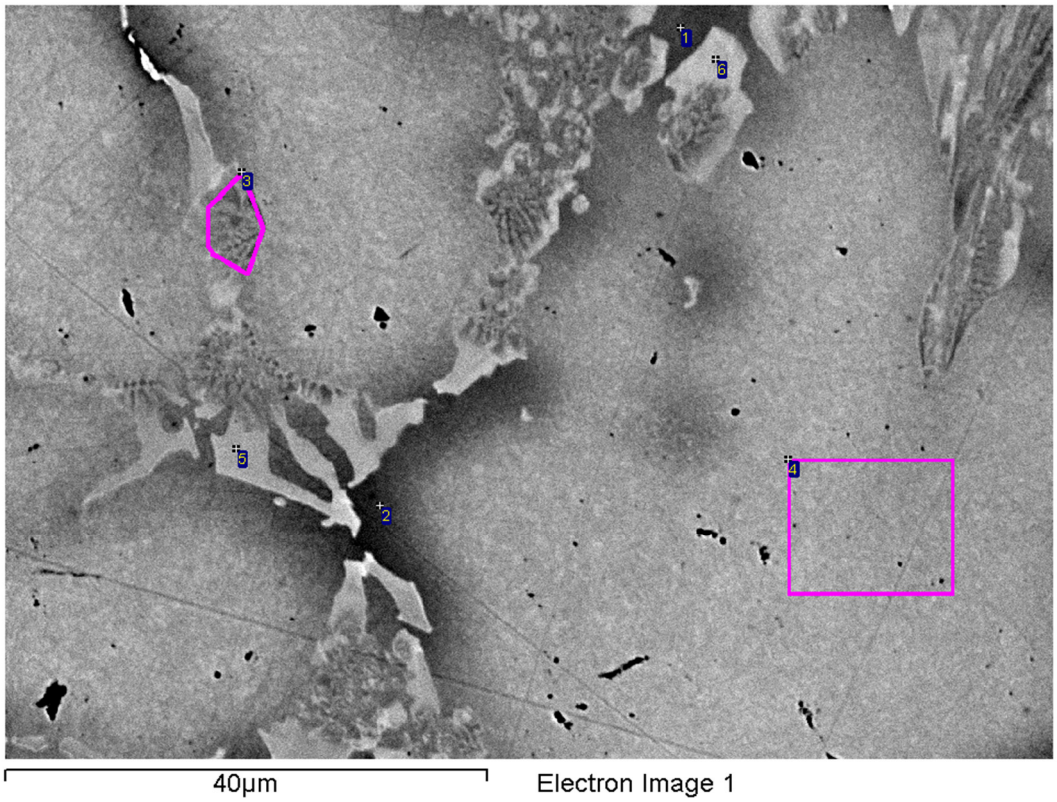

(**a**)

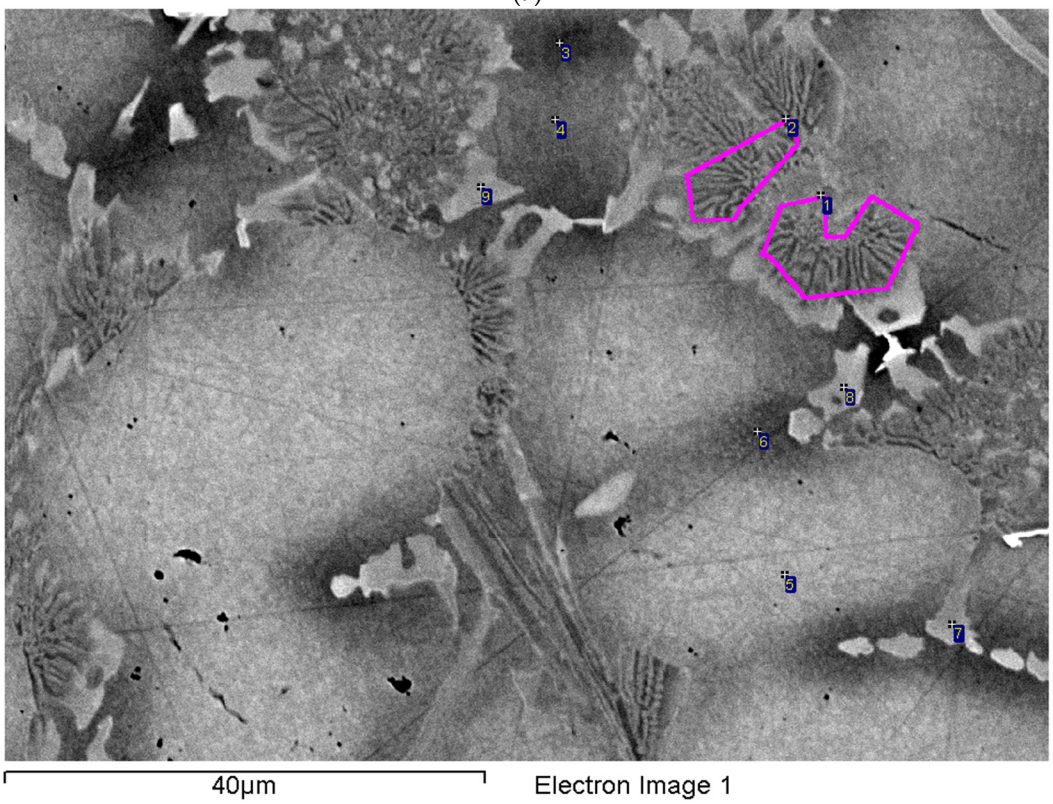

(**b**)

Figure 3. *Cont*.

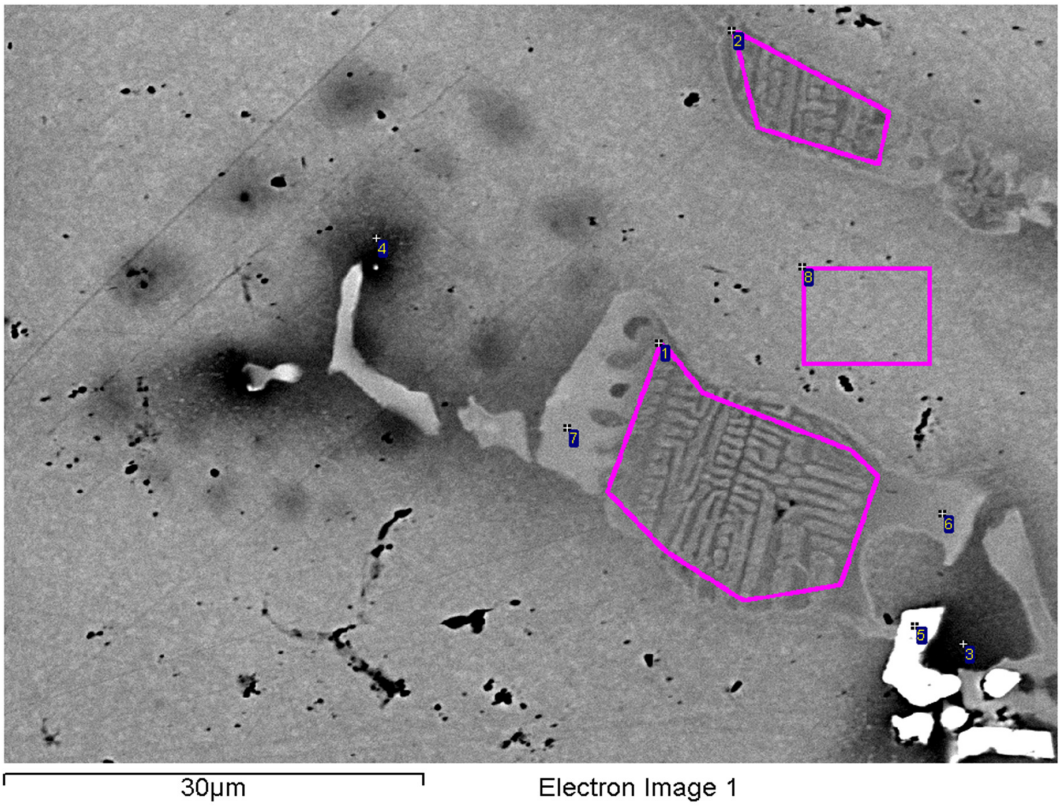

(**c**)

Figure 3. Details of lamellar microstructure and composition (at.%) of phases in the bulk of NV1-AC. (**a**) Analyses 1 to 6 as follows: 1: solid solution 42.8Nb-30.6Ti-1.7Si-5.9Al-4.1Cr-5.1Hf-2.9Sn-6.9V, 2: solid solution 38.1Nb-31.7Ti-2.2Si-5.7Al-6.1Cr-5.7Hf-2.7Sn-7.8V, 3: lamellar microstructure 39.2Nb-22.7Ti-19.7Si-4.4Al-1.1Cr-8.2Hf-1.3Sn-3.4V,<Si> = 25.4 at.%, 4: solid solution 58.5Nb-21.6Ti-2Si-5.2Al-1.9Cr-4.4Hf-2.3Sn-4.1V, 5: 5-3 silicide 23.1Nb-22.2Ti-35.3Si-3.2Al-0.7Cr-13.1Hf-0.5Sn-1.9V, Nb/(Ti + Hf) = 0.65, <Si> = 39 at.%, 6: 5-3 silicide 23Nb-21.9Ti-35.5Si-3.5Al-0.5Cr-13.3Hf-0.4Sn-1.9V, Nb/(Ti + Hf) = 0.65, <Si>= 39.4 at.%. (**b**) Analyses 1 to 8 as follows: 1: lamellar microstructure 40.2Nb-23.9Ti-17.5Si-4.6Al-1.3Cr-7.3Hf-1.6Sn-3.6V, <Si> = 23.7 at.%, 2: lamellar microstructure 39.2Nb-23.1Ti-18.6Si-4.8Al-1.2Cr-7.7Hf-1.6Sn-3.8V, <Si> = 25 at.%, 3: solid solution 40.2Nb-31.3Ti-1.5Si-6.1Al-5Cr-4.9Hf-3.1Sn-7.9V, 4: solid solution 48.5Nb-26.7Ti-2.5Si-5.4Al-3.9Cr-4.9Hf-2.6Sn-6.4V, 5: solid solution 60.3Nb-20.9Ti-1.8Si-5Al-1.3Cr-4.3Hf-2.3Sn-4.1V, 6: solid solution 41.7Nb-29.6Ti-2.6Si-5.8Al-4.3Cr-5.6Hf-2.8Sn-7.6V, 7: 5-3 silicide 22Nb-23Ti-35Si-3.6Al-0.7Cr-13Hf-0.4Sn-2.3V, Nb/(Ti + Hf) = 0.61, <Si > =39 at.%, 8: 5-3 silicide 24.5Nb-21.6Ti-35.5Si-3.6Al-0.4Cr-12.4Hf-0Sn-2V, Nb/(Ti + Hf) = 0.72, <Si> = 39.1 at.%, 9: 5-3 silicide 24.1Nb-22.1Ti-35.3Si-3.5Al-0.4Cr-12.4Hf-0.4Sn-1.8V, Nb/(Ti + Hf) = 0.7, <Si> = 39.2 at.%. (**c**) Analyses 1 to 8 as follows: 1: lamellar microstructure 40.1Nb-22.7Ti-18.3Si-4.7Al-1.3Cr-7.7Hf-1.6Sn-3.6V, <Si> = 24.6 at.%, 2: lamellar microstructure 38.7Nb-23Ti-20.1Si-4.4Al-1.1Cr-8Hf-1.4Sn-3.3V, <Si> = 25.9 at.%, 3: solid solution 38Nb-33.2Ti-1.5Si-5.5Al-6.6Cr-4.1Hf-3Sn-8.1V, 4: solid solution 38.3Nb-32Ti-2Si-5.8Al-5.8Cr-5Hf-3Sn-8.1V, 5: hafnia 34Hf-66O, 6: 5-3 silicide 25.6Nb-21.5Ti-35.3Si-3.4Al-0Cr-11.8Hf-0.4Sn-2V, Nb/(Ti + Hf) = 0.77, <Si> = 39.1 at.%, 7: 5-3 silicide 23.5Nb-22.4Ti-35.3Si-3.4Al-0Cr-12.6Hf-0.5Sn-2.3V, Nb/(Ti + Hf) = 0.67, <Si> = 39.2 at.%, 8: solid solution 59.7Nb-21.2Ti-2.3Si-4.8Al-1.4Cr-4Hf-2.3Sn-4.3V.

The volume fraction of Nb_{ss} in NV1-AC was about 0.8 (Table 1). Data for the average chemical composition of the phases in the whole button/ingot are given in Table 2. Note that the very fine scale of the lamellar structure prevented reliable analysis of the chemical composition of its phases using EPMA. Strong partitioning of Cr, Ti, and V in the solid solution and of Hf and Ti in the silicide, which led to varying BSE contrast at the interface between these phases, was noted (Figures 2 and 3).

Table 2. EPMA data (at.%) of phases in NV1-AC and the bulk of NV1-HT. (Average values are shown in bold numbers).

Phases in NV1-AC	Elements								
	Nb	**Ti**	**Si**	**Al**	**Cr**	**Hf**	**Sn**	**V**	**O**
Nb_{ss}	56.0–65.3	14.4–23.5	1.3–2.9	4.2–5.5	0.3–2.2	3.4–4.4	1.7–2.5	3.3–5.2	-
	60.6 ± 2.8	**20.9** ± 1.2	**2.0** ± 0.4	**4.9** ± 0.3	**1.5** ± 0.5	**3.8** ± 0.3	**2.1** ± 0.2	**4.2** ± 0.4	-
Ti-rich Nb_{ss}	40.3–51.9	25.5–34.0	1.6–2.7	5.4–6.1	2.0–5.0	3.2–4.9	2.2–3.0	5.2–7.0	-
	47.5 ± 3.3	**28.4** ± 2.8	**2.2** ± 0.4	**5.7** ± 0.2	**3.3** ± 0.8	**4.3** ± 0.5	**2.8** ± 0.2	**5.8** ± 0.6	-
Ti, Cr, and V-rich Nb_{ss}	29.8–45.0	28.5–35.7	1.4–1.7	5.1–6.1	3.6–8.4	4.5–6.0	2.4–2.8	7.8–10.2	-
	36.5 ± 3.9	**32.8** ± 1.7	**1.6** ± 0.2	**5.6** ± 0.3	**6.8** ± 1.1	**5.3** ± 0.5	**2.7** ± 0.3	**8.7** ± 0.8	-
Nb_5Si_3	33.8–36	18.8–20.8	31.9–33.4	3.7–4.1	0.2–1.0	6.0–7.0	0.6–1.0	1.2–2.0	
	34.8 ± 0.9	**19.3** ± 0.8	**32.7** ± 0.7	**3.8** ± 0.2	**0.5** ± 0.3	**6.4** ± 0.4	**0.8** ± 0.1	**1.7** ± 0.3	
Ti and Hf-rich Nb_5Si_3	14.9–25.3	22.4–25.4	34.1–35.6	3.1–4.4	0.2–1.2	12.0–17.0	0.1–0.5	1.4–2.9	-
	21.6 ± 2.8	**23.4** ± 1.2	**34.8** ± 0.5	**3.6** ± 0.3	**0.6** ± 0.4	**13.6** ± 1.2	**0.3** ± 0.2	**2.1** ± 0.3	-
Ti-rich Nb_5Si_3 *	23.2–36.0	18.8–23.0	31.9–35.4	3.4–4.0	0.2–1.0	6.0–13.2	0.2–0.9	1.2–2.6	-
	29.2 ± 4.8	**20.7** ± 1.3	**34.1** ± 1.2	**3.7** ± 0.2	**0.4** ± 0.3	**9.6** ± 2.3	**0.5** ± 0.3	**1.8** ± 0.3	-
Lamellar * Nb_{ss} + Nb_5Si_3	37.7–40.6	21.8–25.1	16.6–21.6	4.1–4.8	0.9–1.8	7.2–8.9	1.1–1.7	2.8–4.1	-
	39.3 ± 0.5	**23.2** ± 0.8	**19.1** ± 1.4	**4.5** ± 0.2	**1.3** ± 0.2	**7.8** ± 0.3	**1.5** ± 0.2	**3.3** ± 0.3	-
HfO_2	-	-	-	-	-	33.4–34.5	-	-	65.5–66.6
						34.0 ± 0.3			**66.0** ± 0.3
NV1-HT									
Nb_{ss}	54.7–56.4	22.8–24.1	0.9–1.5	5.0–6.1	4.5–5.6	3.3–4.2	2.0–2.8	2.0–2.6	-
	55.6 ± 0.5	**23.6** ± 0.4	**1.2** ± 0.2	**5.6** ± 0.3	**5.2** ± 0.2	**3.8** ± 0.3	**2.6** ± 0.2	**2.4** ± 0.3	-
Nb_5Si_3	25.1–26.8	19.2–20.2	35–36.6	3.4–4.0	1.5–2.2	11.8–13.8	0.1–0.4	0.2–0.6	-
	25.8 ± 0.5	**19.6** ± 0.4	**35.7** ± 0.5	**3.7** ± 0.2	**1.6** ± 0.2	**13.0** ± 0.8	**0.2** ± 0.1	**0.4** ± 0.1	-
HfO_2	-	-	-	-	-	33.0–33.8	-	-	66.2–67.0
						33.5 ± 0.5			**66.5** ± 0.5

* see text.

For example, in Figure 2a,b, the areas of darker contrast near the Nb_5Si_3 silicide are Ti rich, and the brighter contrast Nb_5Si_3 grains are Hf rich (see below). The Ti-rich Nb_5Si_3, regarding its high Ti concentration, corresponded to the Ti-rich Nb_5Si_3 reported in other Ti-containing RM(Nb)ICs [35,36]. The Ti-rich Nb_{ss} was observed only in the top and bottom of NV1-AC. In Table 2, the Nb_5Si_3 is also designated as Ti- and Hf-rich Nb_5Si_3, owing to its high Hf and Ti contents (see below).

Compared with the nominal composition, the NV1-AC was slightly richer in Si with an average concentration of 6.2 at.%. The concentrations of the other alloying elements were very close to the nominal ones (see Section 2). There was macrosegregation of Ti and Si, the concentrations of which were in the ranges: 19.4 to 24.3 at.% (MACTi = 4.9 at.%) and 3.9 to 7 at.% (MACSi = 3.1 at.%), respectively. The XRD (Figure 1a) indicated the presence of tetragonal αNb_5Si_3 and hexagonal 5-3 silicide. There were three peaks that are characteristic of αNb_5Si_3 compared with six peaks for the hexagonal γNb_5Si_3 and four peaks for the hexagonal Ti_5Si_3, all shared with other phases. The latter two silicides are isomorphous [24].

In the areas close to the top of the button/ingot, the Si concentration was in the range 3.9 to 5.9 at.%, and the microstructure consisted of Nb_{ss}, Nb_5Si_3, and a lamellar microstructure of these phases. The Ti-rich Nb_{ss} was found either next to the Ti-and-Hf-rich Nb_5Si_3, or surrounded the HfO_2, which was often found adjacent to the Ti-and-Hf-rich Nb_5Si_3. The Ti-rich areas in the Nb_{ss} and the Ti-rich Nb_5Si_3 exhibit a dark contrast in the microstructures shown in the Figure 2a,b. However, the Ti- and Hf-rich areas in the Nb_5Si_3 exhibited bright contrast. The Ti concentration varied from 18.8 to 20.8 at.% in the Ti-rich Nb_5Si_3 and from 22.4 to 25.2 at.% in the Ti-and-Hf-rich Nb_5Si_3. Despite the fact that the Ti-and-Hf-rich Nb_5Si_3 was richer in Ti compared with the Ti-rich Nb_5Si_3, it exhibited a brighter contrast owing to its very high Hf concentration, which varied from 12 to 12.7 at.% compared with 6 to 7 at.% in the Ti-rich Nb_5Si_3. The aforementioned Ti-rich and Ti-and-Hf-rich Nb_5Si_3 was observed more often as two discrete grains in the top of the ingot, unlike the bulk and bottom of the ingot where the segregation of Hf and Ti was observed mainly at the exterior or the interior of a single Nb_5Si_3 grain. The lamellar microstructure

of Nb_{ss} and Nb_5Si_3 was formed adjacent to the Ti-and-Hf-rich Nb_5Si_3. The solubility of Cr in Nb_5Si_3 was low and exceeded 1 at.% in the Ti-and-Hf-rich Nb_5Si_3. Similarly, the V concentration in the Nb_5Si_3 was low and varied from 1.4 to 2.9 at.% in the Ti-and-Hf-rich Nb_5Si_3 and from 1.2 to 2.6 at.% in the Ti-rich Nb_5Si_3.

In the bulk of the button/ingot, the Si concentration was in the range 5.8 to 7 at.%. The microstructure was slightly coarser and consisted of the same phases as in the top (Figure 2b) but with two main exceptions. Firstly, the Ti-rich parts of the Nb_{ss} were also rich in V and Cr where the concentrations of these elements varied from 7.8 to 10.2 at.% and 3.6 to 8.4 at.%, respectively. This Nb_{ss} is designated as Ti-, V-, and Cr-rich Nb_{ss} in Table 2. The solubility of Al, Si, and Sn in the Nb_{ss} was reduced. Secondly, the Nb_5Si_3 exhibited Ti- and Hf-rich areas in different parts of the same grain. The Ti-rich Nb_5Si_3, unlike that observed in the top of the ingot, was also rich in Hf, and the Ti-and-Hf-rich Nb_5Si_3 was observed with Hf concentrations as high as 17 at.%. In other words, the Hf solubility in Nb_5Si_3 was much higher in the bulk of the ingot, compared with the top. Differences in the composition of the 5-3 silicide should also be noted (compare composition of 5-3 silicide in Figures 2b and 3). The solubility of Sn was negligible in both the Ti-and-Hf-rich and the Ti-rich Nb_5Si_3. The lamellar microstructure (Figure 3) had average composition 39.6Nb-23.4Ti-18.2Si-7.7Hf-4.6Al-3.6V-1.6Sn-1.3Cr (at.%), similar to that observed in the top of the ingot.

In the bottom of the ingot, the Si concentration was in the range of 4.9 to 6.6 at.%. The Ti-rich Nb_{ss} had a similar composition to that in the top. In the Nb_5Si_3, the Hf segregation was not as strong as in the bulk. The solubility of Al in the Nb_{ss} was as high as 6.1 at.%. The average Si concentration in the lamellar microstructure was 20.8 at.%, which was slightly higher compared with the top and bulk of the ingot.

4.2. Heat-Treated (NV1-HT)

The actual chemical composition of NV1-HT was Nb-23.3Ti-5Si-4.9Al-1.8Cr-5Hf-2Sn-3.7V. The XRD data (Figure 1b) suggested the presence of αNb_5Si_3 and hexagonal 5-3 silicides and Nb_3Si. However, the presence of Nb_3Si in the microstructure was not confirmed by exhaustive study using EPMA. Compared with NV1-AC, the number of peaks for αNb_5Si_3 and γNb_5Si_3 and Ti_5Si_3 had increased and decreased, respectively. The typical microstructure in the bulk of NV1-HT consisted of Nb_{ss}, Nb_5Si_3, and HfO_2 (see Figure 2d). There was no evidence of the lamellar microstructure seen in NV1-AC. Homogenisation had taken place in both the Nb_{ss} and Nb_5Si_3 (Table 2). The HfO_2 was found at the interface of Nb_{ss} and Nb_5Si_3. The vol.% of the Nb_{ss} had not changed significantly compared with NV1-AC (see Table 1). The Cr solubility in the Nb_{ss} increased after the heat treatment and was as high as 5.6 at.% in some parts of the solid solution. On the contrary, the average solubility of V in the Nb_{ss} had decreased to 2.4 at.%. The Ti concentration in the Nb_{ss} was about 23.6 at.%, close to the nominal Ti concentration in the alloy. The solubilities of Al, Sn, and Hf in the Nb_{ss} did not change after the heat treatment. The solubilities of Ti and V in the Nb_5Si_3 were reduced, while those of Al and Hf had not changed. However, the solubility of Cr had increased in the Nb_5Si_3.

In the microstructure near the surface of NV1-HT there were Ti-rich regions in the Nb_5Si_3 (see Table 3). This was not observed in the bulk of NV1-HT (Table 2). Furthermore, the Hf concentration in the Nb_5Si_3 was reduced compared with the Nb_5Si_3 in the bulk of NV1-HT and NV1-AC (Tables 2 and 3), and the Ti concentration in the Ti-rich Nb_5Si_3 was similar to that of the Ti- and Hf-rich Nb_5Si_3 in NV1-AC, while in the Nb_5Si_3, the average Ti and Hf concentrations barely exceeded 15 and 1 at.%, respectively. Thus, near the surface area of NV1-HT the Nb_5Si_3 had Nb/(Ti + Hf) greater than one, whereas in the bulk, this ratio was less than one. No Hf was analysed in the Nb_{ss}, and the Al, V, Cr, and Sn concentrations were in the solubility range of these elements as in the Ti-rich Nb_{ss} in NV1-AC. The vol.% and the size of the Hf oxide particles had increased compared with the bulk of NV1-HT (Figure 2c,d). Together with the phases described above, Ti nitride

of irregular shape and various sizes had formed near the surfaces of NV1-HT specimens (Figure 2c), up to about 1 mm below the surface.

Table 3. EPMA data (at.%) of the phases in the microstructure near the surface of NV1-HT (1500 °C/100 h). (Average values are shown in bold numbers).

Phases Near Surface of NV1-HT	Element									
	N	**O**	**Nb**	**Ti**	**Si**	**Al**	**Cr**	**Hf**	**Sn**	**V**
Nb_{ss}	-	-	63.0–63.4	18.4–19.6	0.1–0.5	6.0–6.2	2.7–2.9	-	2.4–2.5	6.0–6.2
	-	-	**63.2** ± 0.3	**19.0** ± 0.8	**0.3** ± 0.2	**6.1** ± 0.1	**2.8** ± 0.2	-	**2.5** ± 0.1	**6.1** ± 0.1
Nb_5Si_3	-	-	45.9–46.1	14.8–15.2	33.6–34.0	1.8–2.1	-	1.2–1.4	0.5–0.7	1.0–1.3
	-	-	**46.1** ± 0.1	**15.0** ± 0.2	**33.8** ± 0.2	**2.0** ± 0.1	-	**1.3** ± 0.2	**0.6** ± 0.1	**1.2** ± 0.2
Ti-rich Nb_5Si_3	-	-	32.5–33.5	23.3–24.3	33.2–33.5	3.4–3.8	0.4–0.5	2.5–3.9	-	2.2–2.5
	-	-	**33** ± 0.4	**23.9** ± 0.5	**33.4** ± 0.2	**3.6** ± 0.2	**0.4** ± 0.1	**3.3** ± 0.6	**-**	**2.4** ± 0.1
HfO_2	-	65.6–68.2	-	-	-	-	-	31.8–34.4	-	-
	-	**67.1** ± 1.1	-	-	-	-	-	**32.9** ± 1.1	-	-
Ti nitride	34.5–40.9	-	2.6–3.4	54.8–61.3	-	-	-	0.6–1.7	-	-
	36.9 ± 2.4	-	**3.0** ± 0.2	**59.0** ± 2.3	-	-	-	**1.1** ± 0.4	-	-

The Ti nitride grains were found either adjacent to Nb_5Si_3 or between the Nb_5Si_3 and HfO_2. The presence of Ti nitride was confirmed only by EPMA (Table 3) owing to its small volume fraction in NV1-HT.

4.3. Oxidation

The mass change of NV1 in isothermal oxidation at 700, 800, and 900 °C was compared with the "reference" MASC alloy (see the introduction) and the alloys NV3 [37], NV4 [38], NV5 [37], NV6 [39], and NV8 [38] in Figure 4. Large button/ingots of all these alloys were made using arc melting. The oxidised specimens are shown in Figure 5, and the oxidation rate constants are given in Table 4. In the latter table, the vol.% of Nb_{ss} in the Sn-containing alloys with similar Ti concentration to the MASC alloy is also given. Note (i) that the MASC alloy was Sn-free, (ii) that the vol.% Nb_{ss} of the alloy NV4 [38] was about 51.3%, (iii) that the alloy NV4 was very Ti-rich (45 at.%, nominal), and (iv) that the Sn content of the alloys NV3 to NV6 and NV8 was 5 at.% (nominal) compared with 2 at.% Sn in NV1 (for nominal composition of the alloys, see the Table 1 in the Appendix A). The alloy NV9 [39] suffered catastrophic pest oxidation at all three temperatures. Data for this alloy is not included in the Figure 4. Furthermore, because of (iii), data for the oxidation rate constants of the alloy NV4 is not included in the Table 4.

Table 4. Oxidation rate constants of the alloys NV1, NV3, NV4, NV5, NV6, and NV8 at 700 °C, 800 °C, and 900 °C.

Alloy	Vol.% Nb_{ss}	700 °C		800 °C		900 °C
		k_l ($g \cdot cm^{-2} \cdot s^{-1}$)	k_p ($g^2 \cdot cm^{-4} \cdot s^{-1}$)	k_l ($g \cdot cm^{-2} \cdot s^{-1}$)	k_p ($g^2 \cdot cm^{-4} \cdot s^{-1}$)	k_l ($g \cdot cm^{-2} \cdot s^{-1}$)
NV1	79.6	-	$3.4 \cdot 10^{-11}$	-	$2.8 \cdot 10^{-10}$	$5.4 \cdot 10^{-8}$ (0–16 h), $1.3 \cdot 10^{-7}$ (>16 h)
NV3	28	-	$1.4 \cdot 10^{-11}$	$1.4 \cdot 10^{-7}$	-	$1.4 \cdot 10^{-7}$
NV5	1.9	-	$1.3 \cdot 10^{-12}$	-	$1.3 \cdot 10^{-12}$	$3.0 \cdot 10^{-7}$ (0–55 h), $1.3 \cdot 10^{-7}$ (>55 h)
NV6	33.5	-	$1.3 \cdot 10^{-11}$	$3.3 \cdot 10^{-8}$	-	$2.1 \cdot 10^{-6}$ (0–17 h), $9.3 \cdot 10^{-8}$ (>17 h)
NV8	15.3	-	$7.2 \cdot 10^{-12}$	-	$6.1 \cdot 10^{-11}$	$3.1 \cdot 10^{-7}$ (0–5 h), $9.8 \cdot 10^{-7}$ (>5 h)
MASC	30	$5.6 \cdot 10^{-8}$ (>10 h)	$6.9 \cdot 10^{-12}$ (0–10 h)	$1.5 \cdot 10^{-7}$	-	$5.3 \cdot 10^{-7}$

At 700 °C, the NV series of alloys (see the previous paragraph and the Table 1 in the Appendix A) followed parabolic oxidation kinetics, whereas the MASC alloy exhibited parabolic oxidation for the first 10 h and then linear oxidation until the end of the oxidation (Table 4). The ranking of alloys from best to worst oxidation was NV5, NV8, NV6, NV3, NV1, and MASC. Partial pest oxidation was observed only for the MASC alloy (Figure 4). The NV1 alloy did not pest; there was some "blistering" along its edges; and its mass change was 3.5 mg/cm^2. At 800 °C, the alloys NV3, NV6, and MASC followed linear

oxidation kinetics, and the alloys NV1, NV2, NV5, and NV8 followed parabolic oxidation kinetics. The ranking of alloys from best to worst oxidation was NV5, NV8, NV1, NV6, MASC, and NV3. Pest oxidation was observed only for the NV3 alloy. The MASC alloy formed a Maltese cross (Figure 4). Even though the specimen of the NV1 alloy did not pest, there was evidence of oxide growth around one of the specimen corners (see the bottom left-hand corner in Figure 4), and some oxide from this area spalled off. The mass change of NV1 was 10 mg/cm^2. At 900 °C, all the alloys followed linear oxidation. The ranking of alloys from best to worst oxidation was NV1, NV3, NV5, NV6, MASC, and NV8. Pest oxidation was observed for the alloys NV6 and NV8. The MASC alloy had formed a Maltese cross that separated in six pieces and a small core (Figure 4). The mass change of NV1 was 30 mg/cm^2 after 70 h, and its scale spalled off.

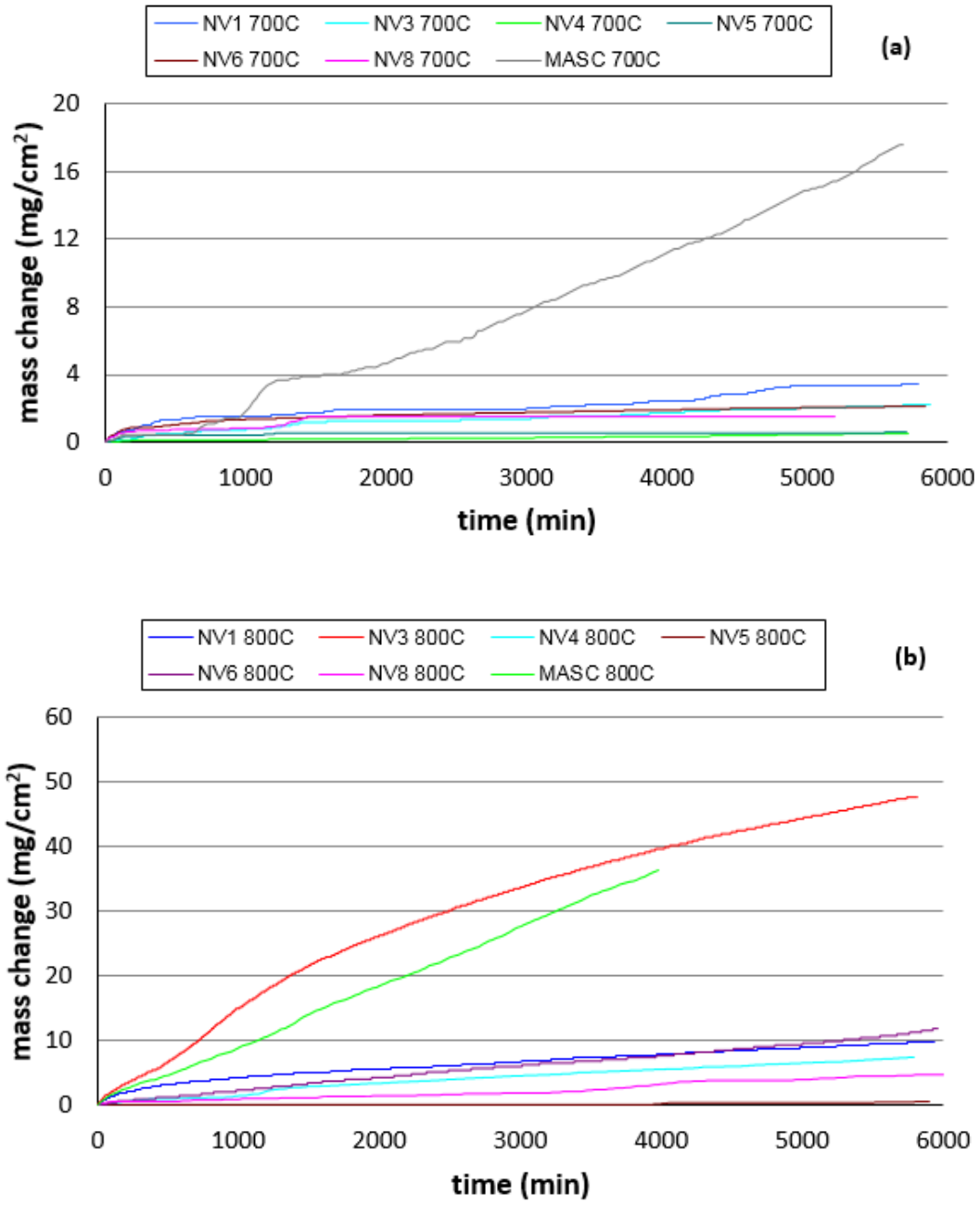

Figure 4. *Cont*.

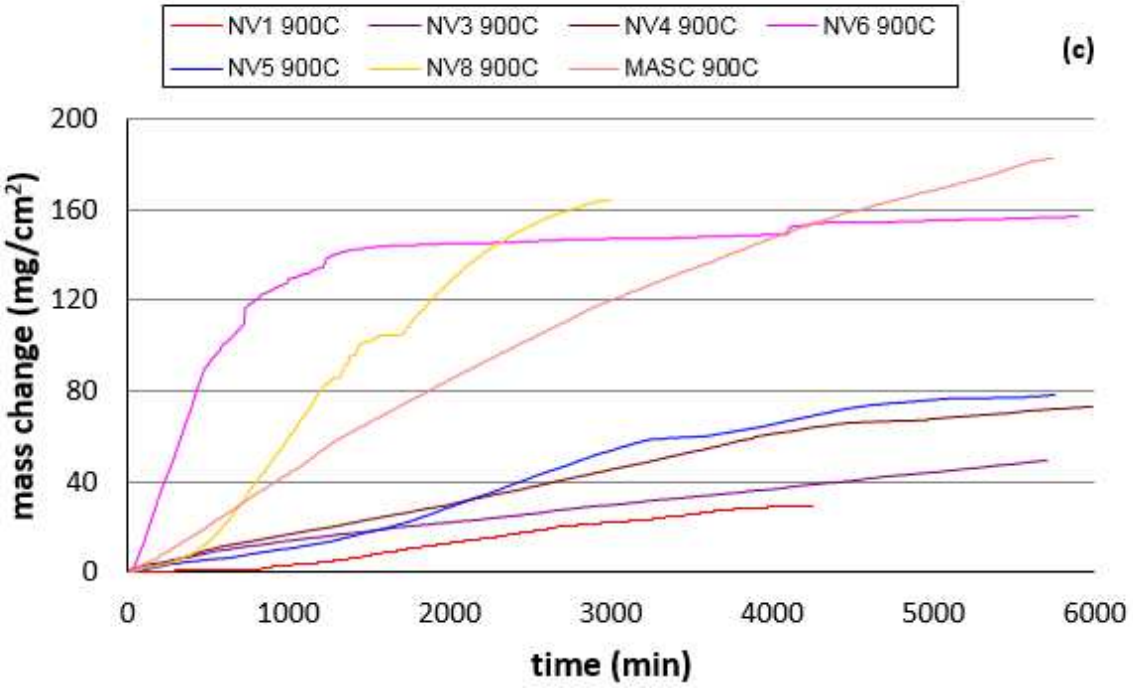

Figure 4. Mass change versus time of the alloys NV1, NV3, NV4, NV5, NV6, and NV8 at (**a**) 700 °C, (**b**) 800 °C, and (**c**) 900 °C. Ranking of alloys from best to worst oxidation in (**a**) NV4, NV5, NV8, NV6, NV3, NV1, and MASC; (**b**) NV5, NV8, NV4, NV1, NV6, MASC, and NV3; and (**c**) NV1, NV3, NV4, NV5, NV6, MASC, and NV8.

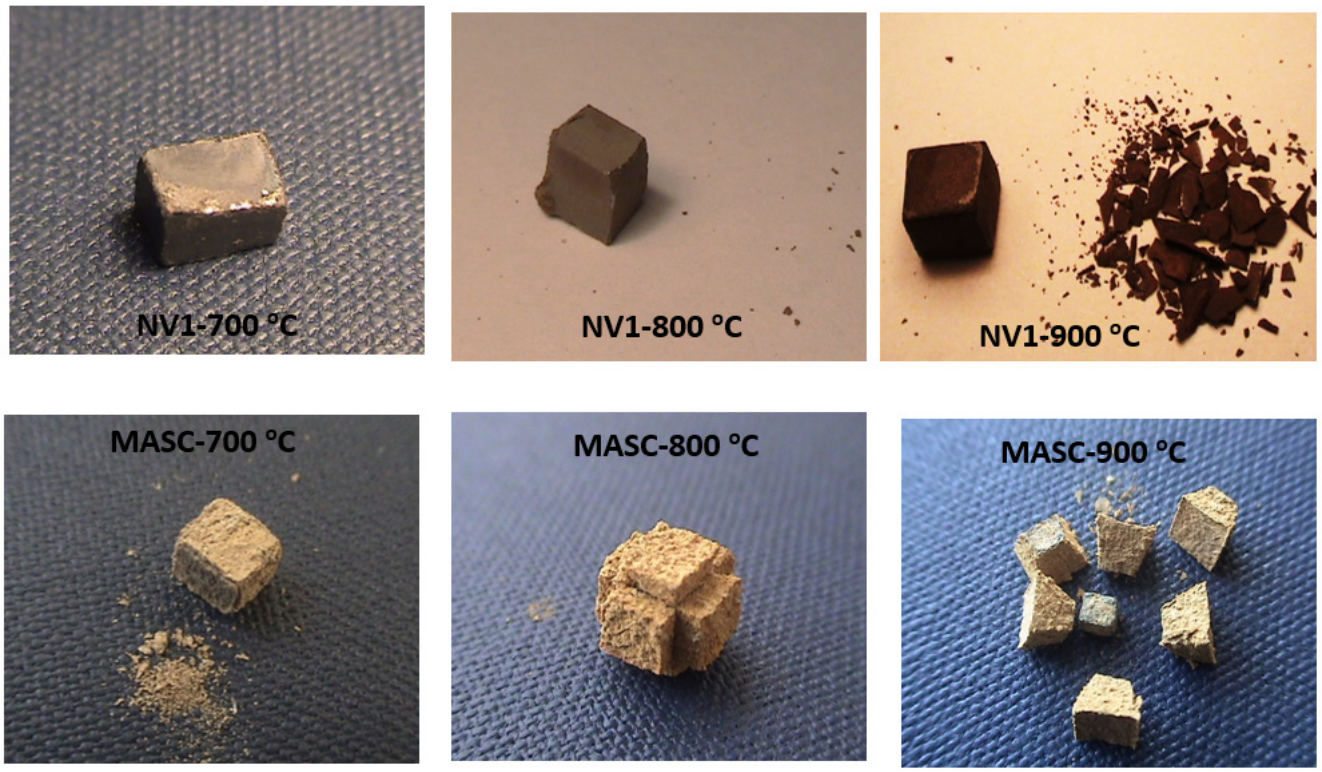

Figure 5. The oxidised specimens of the alloys NV1 (top row) and MASC (bottom row) at 700, 800, and 900 °C.

The oxidised specimens of the alloy NV1 at 800 and 900 °C were studied using XRD and EPMA. The actual composition of the bulk of NV1 at 800 °C was 34.8Nb-14.9Ti-3.9Si-3.6Al-2.4Cr-3.7Hf-1.4Sn-1.4V-33.9O. The alloy was heavily contaminated with oxygen. The scale that separated from the specimen during isothermal oxidation at 900 °C for

100 h (Figure 4) was crushed and then studied using XRD. The latter showed peaks that corresponded to the Nb_2O_5, $TiNbO_4$, $Nb_2O_5{\cdot}TiO_2$, $3Nb_2O_5{\cdot}TiO_2$, $5Nb_2O_5{\cdot}2TiO_2$, $CrNbO_4$, $AlNbO_4$, SiO_2, TiO_2, and HfO_2 oxides (Figure 6). The same oxides were observed at 800 °C. The cross section of the oxidised specimen at 800 °C was studied by EPMA. The EPMA analysis data is given in Table 5. The microstructures of the oxide scale and bulk are shown in Figure 7. Table 6 summarises the phases and characteristic features of the oxidised alloy.

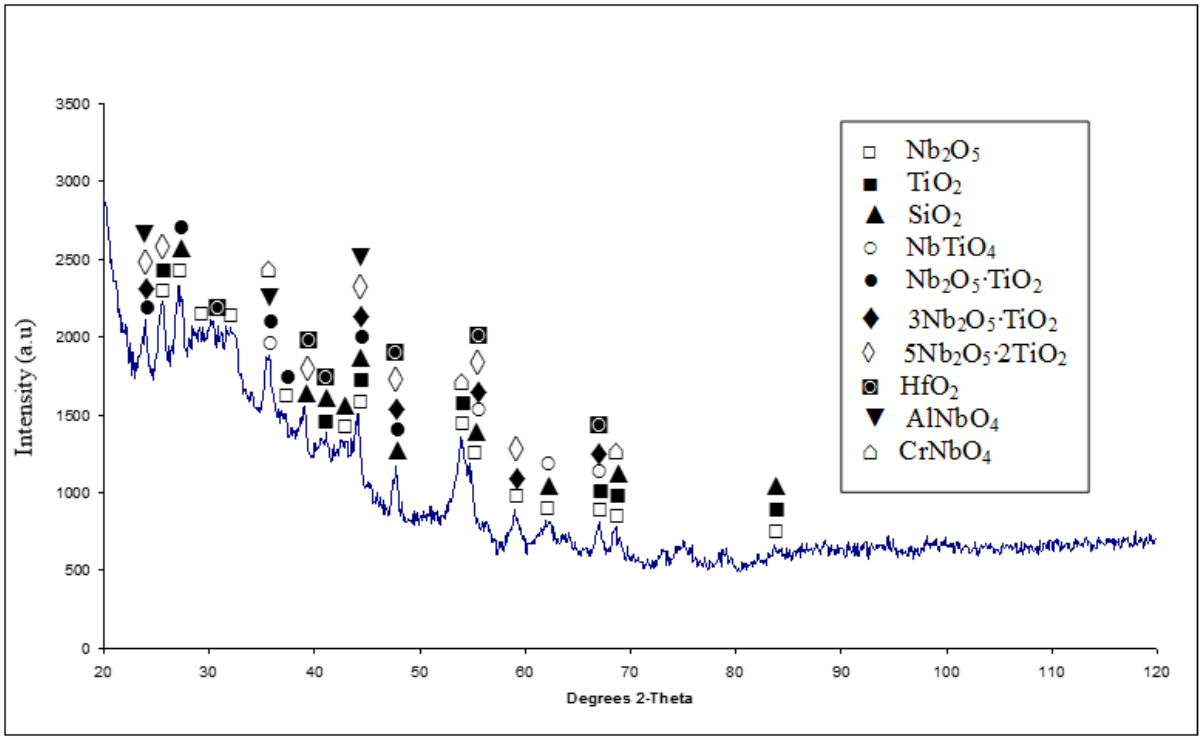

Figure 6. X-ray diffractogram of the oxides formed on NV1 after isothermal oxidation in static air at 900 °C for 100 h.

Table 5. Chemical composition (at.%) of the phases present in the oxide scale and the bulk of the oxidised alloy NV1 at 800 °C/100 h. (Average values are shown in bold numbers).

Phase	Oxide Scale								
	Element								
	Nb	**Ti**	**Si**	**Al**	**Cr**	**Hf**	**Sn**	**V**	**O**
Nb- and Ti-rich oxide	18.9–22.3	5.2–7.8	0.6–0.9	1.4–2.0	0.2–0.8	1.1–1.5	0.2–0.9	1.0–1.8	65.8–68.3
	19.9 ± 0.7	**7.0** ± 0.4	**0.7** ± 0.1	**1.7** ± 0.2	**0.5** ± 0.2	**1.3** ± 0.2	**0.5** ± 0.2	**1.3** ± 0.2	**67.1** ± 0.7
Si-rich oxide	8.2–9.5	6.2–12.0	9.2–12.4	1.0–1.2		3.0–4.3	0.2–0.5	0.4–0.8	64.0–67.4
	9.1 ± 0.3	**7.5** ± 1.1	**11.4** ± 0.8	**1.1** ± 0.1	-	**3.8** ± 0.6	**0.3** ± 0.1	**0.6** ± 0.1	**66.2** ± 0.5
HfO_2						33.2–33.6			66.4–66.8
						33.4 ± 0.1			**66.6** ± 0.1
	Bulk (analyses up to about 300µm below the scale/substrate interface)								
Nb_{ss}	28.9–45.5	11.5–17.3	1.0–1.7	2.6–4.1	0.7–1.5	2.2–3.1	1.0–1.8	2.0–2.9	22.0–47.5
	36.6 ± 4.2	**13.1** ± 1.5	**1.4** ±0.3	**3.1** ± 0.2	**1.0** ± 0.2	**2.4** ±0.2	**1.4** ± 0.2	**2.4** ± 0.3	**38.6** ± 4.5
Ti-rich Nb_{ss}	23.4–39.1	14.5–20	0.6–1.3	2.6–4.0	1.6–2.6	2.4–3.3	1.2–1.8	3.1–3.9	25.0–48.6
	29.2 ± 3.9	**17.0** ± 2.2	**1.0** ± 0.3	**3.3** ± 0.5	**1.9** ± 0.3	**2.7** ± 0.2	**1.5** ± 0.2	**3.5** ± 0.3	**39.9** ± 5.2
Nb_5Si_3	18.0–26.4	18.3–23.2	29.2–33.4	2.6–4.0	0.1–0.6	9.3–11.4	0.1–0.6	1.3–2.2	6.7–14.5
	22.7 ± 3.1	**20.0** ± 1.5	**31.5** ± 1.1	**3.0** ± 0.3	**0.4** ± 0.1	**10.5** ± 0.7	**0.3** ± 0.2	**1.8** ± 0.3	**9.8** ± 2.8
Nb_5Si_3 Oxygen-free	23.1–29.0	20.1–23.0	35.1–36.0	3.2–3.5	0.1–0.7	10.2–12.5	0.1–0.4	1.4–1.9	
	25.7 ± 2	**21.7** ± 0.6	**35.5** ± 0.2	**3.3** ± 0.1	**0.4** ± 0.2	**11.7** ± 0.7	**0.3** ± 0.1	**1.6** ± 0.2	-
Lamellar Nb_{ss} + Nb_5Si_3	24.5–32.5	16.0–19.0	10.4–15.1	2.9–3.8	0.9–1.5	4.8–6.3	0.9–1.3	2.3–2.8	24.8–33.3
	28.4 ± 2.5	**17.6** ± 1.1	**12.5** ± 1.9	**3.3** ± 0.3	**1.1** ± 0.1	**5.4** ± 0.5	**1.1** ± 0.2	**2.6** ± 0.2	**28.0** ± 4
HfO_2						33.4–34.5			65.5–66.6
						34.0 ± 0.3			**66.0** ± 0.2

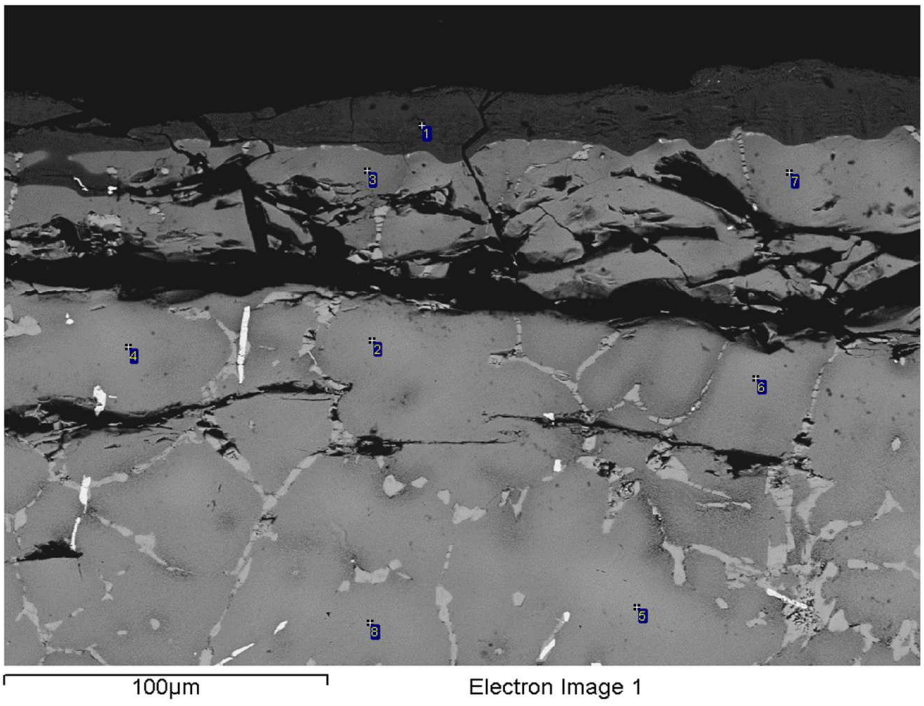

(**a**)

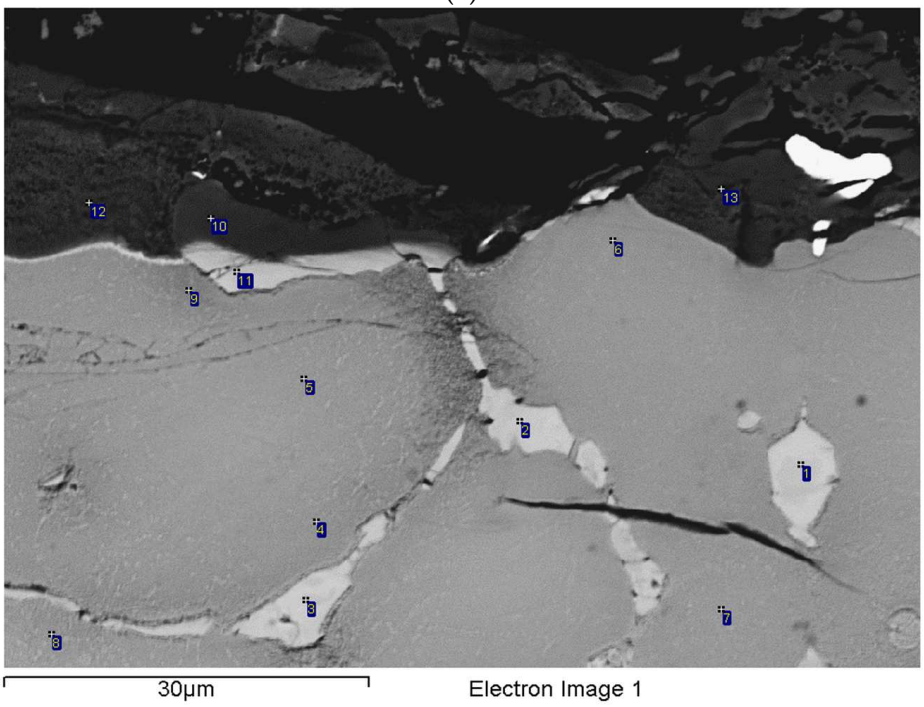

(**b**)

Figure 7. *Cont*.

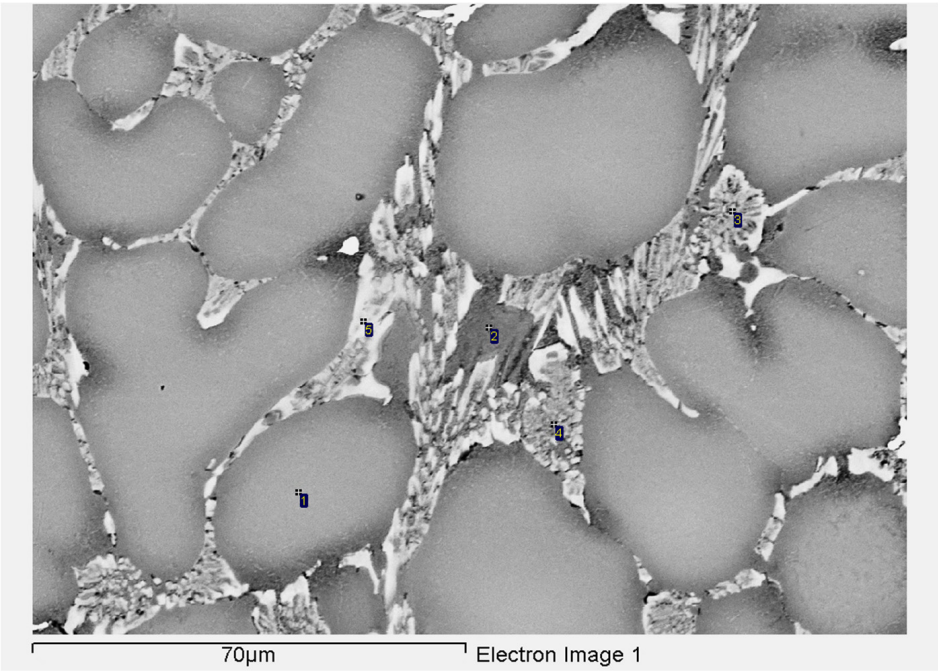

(**c**)

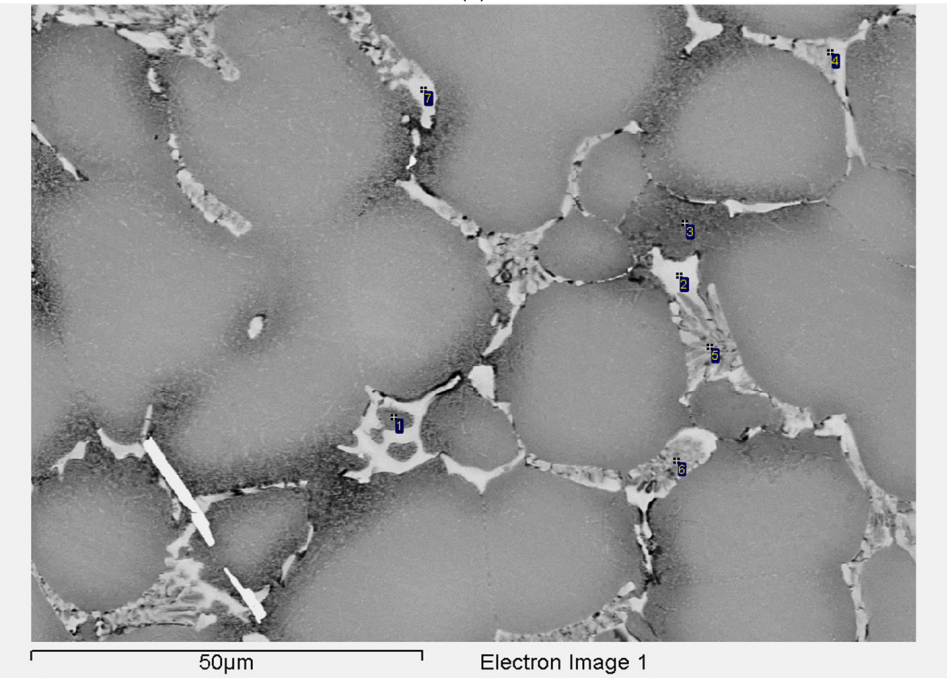

(**d**)

Figure 7. BSE images of the microstructure of NV1 after isothermal oxidation at 800 °C. (**a**) Oxide scale, interface between scale and substrate and bulk of oxidised specimen, 1 scale, 2–8 Nb_{ss}, Nb_5Si_3 is the bright contrast phase. (**b**) Oxide scale and interface between scale and substrate, 1–3 and 11 Nb_5Si_3, 4 to 9 Nb_{ss}, 10 and 13 Si-rich oxide, 12 Nb- and Ti-rich oxide; the thin white contrast phase at the interface of Nb-and-Ti-rich oxide with Nb_{ss} on the left-hand side of analysis 11 is the Sn-rich phase; see text. (**c**) Bulk microstructure: 1 Nb_{ss}; 2 oxidised Nb_{ss}; 3, 4 oxidised lamellar microstructure; 5 Nb_5Si_3. (**d**) Bulk microstructure: 1, 3 Nb_{ss}; 2, 7 Nb_5Si_3; 5, 6 oxidised lamellar microstructure.

Table 6. Phases and characteristic features of the oxide scale and bulk of the oxidised alloy NV1 at 800 °C/100 h.

Location	Phases	Characteristic Features
Oxide scale	Nb- and Ti-rich oxide, Si-rich oxide, and HfO_2	Thickness: non-uniform
		Cracks parallel and transverse to oxide surface
		Nb_{ss}, and Nb_5Si_3 "trapped" in scale
Interface between scale and substrate	Sn-rich phase	Very thin discontinuous layer of an Sn-rich phase
Subscale area		Oxidised Nb_{ss} and Nb_5Si_3 Severe oxidation of Ti-rich Nb_{ss} Cracks in Nb_{ss} running parallel to interface between scale and substrate Cracked Nb_5Si_3
Bulk (up to 300 μm below scale)	Nb_{ss}, Nb_5Si_3, lamellar microstructure, and HfO_2	Microstructure architecture same as in as-cast alloy
		Nb_{ss} oxidised Ti-rich areas of the Nb_{ss} oxidised heavily Nb_5Si_3 also oxidised but less severely compared with Nb_{ss}
		In the bulk, some Nb_5Si_3 grains not oxidised Cracks parallel to the surface formed in Nb_5Si_3 grains near the Interface between scale and substrate
		Partial disintegration (break-up) of lamellar microstructure into Nb_{ss} and Nb_5Si_3 owing to the oxidation of the solid solution

The scale was non-uniform, and its thickness was ≤20 μm. Cracks perpendicular to the substrate were formed in the scale, which consisted of Nb- and Ti-rich oxide (Nb/Ti ≈ 2.8), Si-rich oxide (Nb/Ti ≈ 1.2 and Si/Ti ≈ 1.5), and HfO_2 as well as oxidised Nb_{ss} and Nb_5Si_3 (Tables 5 and 6, Figure 7b). The substrate just below the scale was also cracked with cracks running parallel and perpendicular to the surface of the specimen. In some parts of the cross section, about 50 μm below the oxide scale, there was separation of the subscale alloy from the bulk (Figure 7a). Parts of the Ti-rich Nb_{ss} in the subscale alloy were heavily oxidised (oxygen content in the range 30 to 50 at.%; see "peppered" darker contrast area on the right-hand side of analysis point 2 in Figure 7b), and the oxidised Nb_{ss} exhibited cracks running parallel to the interface (Figure 7b).

At 800 °C, and only in very few areas along the scale/substrate interface, a very thin layer was observed that exhibited a very bright contrast under BSE imaging. The thickness of these layers was too small for quantitative analysis. Line scans across such layers confirmed that they were Sn rich (Figure 8). Analysis of such layers became possible after oxidation at 900 °C, where they became more continuous, and their thickness increased. The analyses showed that the bright contrast layer that formed at 900 °C consisted of Nb_3Sn and Nb_6Sn_5 (see Figure 9). The average composition of Nb_3Sn was 30.8Nb-14.8Ti-4.4Si-3.9Al-3.7Hf-20.2Sn-0.7V-21.5O, whereas that of Nb_6Sn_5 was 51.1Nb-1Ti-2.2Si-1.8Al-3.7Hf-39.9Sn-0.3V, i.e., both compounds were Cr free, and the Nb_6Sn_5 was not contaminated with oxygen.

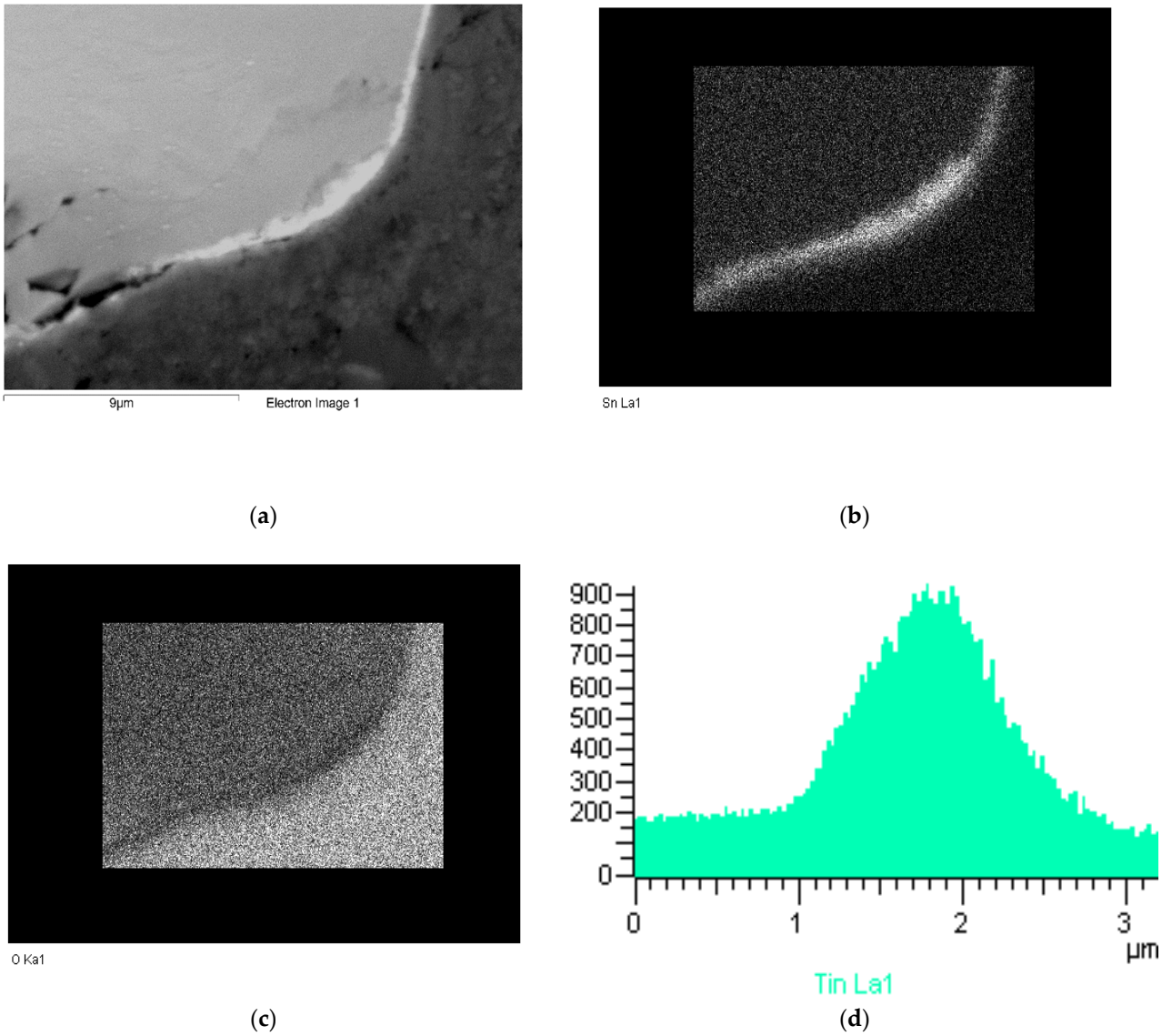

Figure 8. (**a**) Bright contrast layer at the interface between oxide scale and substrate. (**b**) Sn X-ray map. (**c**) Oxygen X-ray map. (**d**) Line scan showing thin layer to be rich in Sn.

The bulk microstructure of the oxidised alloy NV1 consisted of the same phases that were observed in NV1-AC (Figure 7c,d). However, the Nb_{ss} and the Nb_5Si_3 and the lamellar Nb_{ss} + Nb_5Si_3 microstructure were contaminated with oxygen. In some parts of the microstructure, the lamellar microstructure had "disintegrated" (deteriorated and fragmented) owing to the heavy oxidation of its Nb_{ss} (analysis point 4 in Figure 7c). In other words, the contamination of NV1 with oxygen during oxidation had progressed all the way to the bulk. However, in the bulk there were also Nb_5Si_3 grains that were not contaminated with oxygen. In the contaminated Nb_5Si_3, the oxygen concentration varied from about 16 at.% near the oxide scale to about 7 at.% in the bulk of the specimen. On the other hand, the contamination of the Nb_{ss} was most severe. The oxygen content of the Nb_{ss} exceeded 40 at.% in areas up to about 100 µm below the oxide scale, and in the bulk it was about 30 at.%. The Ti-rich Nb_{ss} and Ti-, Cr-, and V-rich Nb_{ss}, which were still observed in the microstructure, exhibited "peppered" darker contrast, and the latter was stronger when the oxygen concentrations approached about 50 at.% (analyses points 2 and 3 in Figure 7c and d, respectively). However, the contamination with oxygen of the bulk of NV1 did not result in a further increase in the volume fraction of HfO_2.

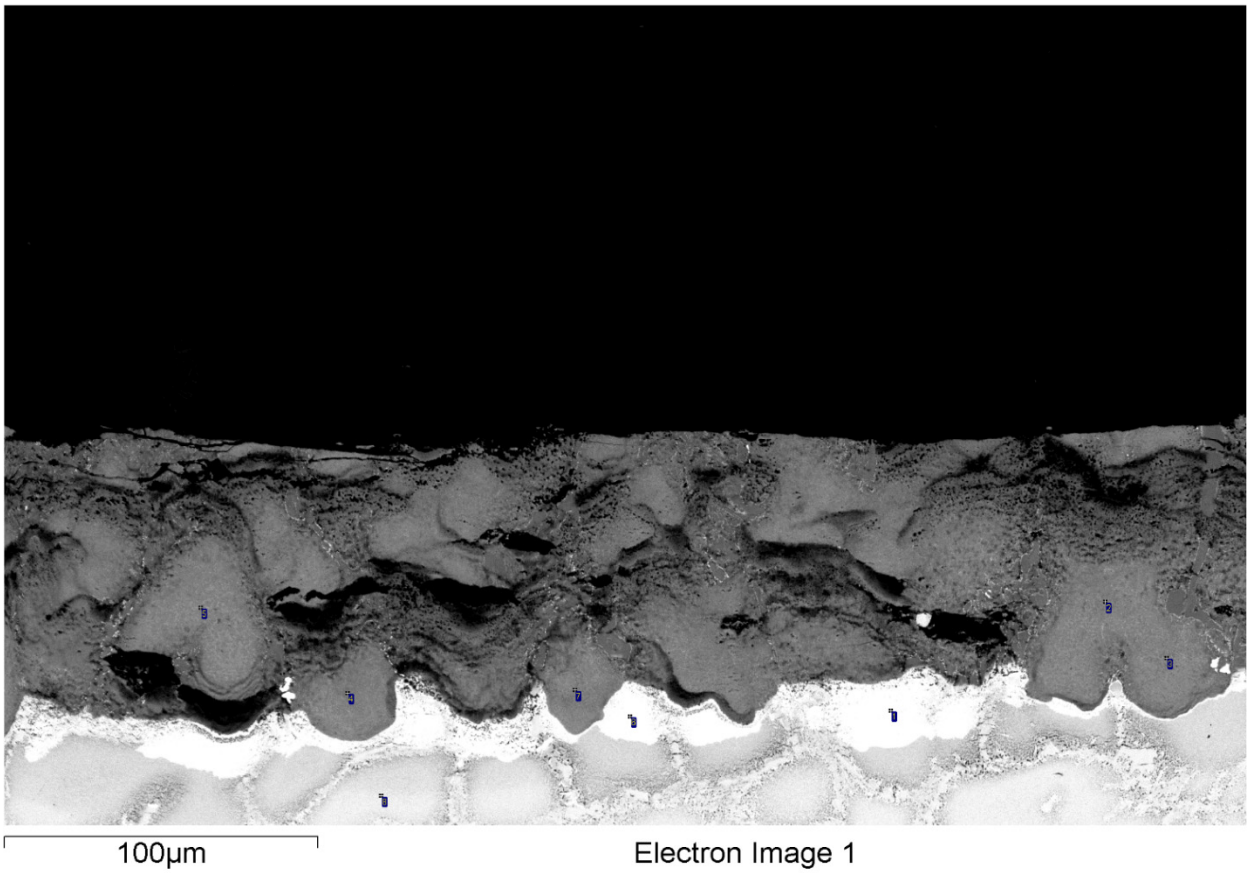

Figure 9. Sn-rich layer formed at the interface between oxide scale and NV1 substrate at 900 °C. Analysis point 1 is on the right-hand side of the bright contrast layer and corresponds to Nb_6Sn_5, whereas the analysis point 6 is on the left-hand side of the point 1 and corresponds to Nb_3Sn. Notice the heavily oxidised areas of Ti-rich Nb_{ss} in the subscale microstructure.

4.4. Hardness and Nano Indentation

The Vickers hardness of the alloy is given in Table 1. The hardness of NV1-HT and of Nb_{ss} in NV1-HT (see below) corresponds to the bulk microstructure (the area contaminated by nitrogen was removed prior to hardness measurements). The hardness decreased slightly after the heat treatment. The average Vickers microhardness of the Nb_{ss} in NV1-AC and NV1-HT, respectively, was 531 HV (516–545) and 540 HV (529–562), where, in the parentheses, the minimum and maximum microhardness values are given.

The large vol.% of Nb_{ss} in NV1 and its characteristic microstructure in NV1-HT (Figure 2d), and in NV1-AC in which in some areas it consisted of Nb_5Si_3 grains between Nb_{ss} grains without a lamellar microstructure (Figure 2b), offered us the opportunity to use nanoindentation to measure the hardness and elastic moduli of said phases in NV1-AC (Figure 10) and NV1-HT (Figure 11). Part (a) in each figure is a 30 × 30 µm^2 AFM image of the indentation area and shows the nanoindentations running from left to right. In parts (b) and (c) in each figure, every point represents a particular nanoindentation. The first indentation on the left-hand side of (b) and (c) in each figure is number 1. In both figures the indentation number 6 is located in Nb_5Si_3, and the indentation number 5 in Figure 10 is on the "interface" between Nb_{ss} and Nb_5Si_3, whereas the indentation numbers 5 and 7 in Figure 11 are on said interface. In both conditions, there was an increase in the modulus at the interface. Additionally, the modulus of Nb_5Si_3 was significantly higher than that of Nb_{ss}. In NV1-AC, there was hardly a change in hardness at the interface, whereas in NV1-HT, a small increase was indicated by the indentation number 7. The hardness and moduli of the Nb_{ss} and Nb_5Si_3 for the as-cast and heat-treated conditions are given in Tables 7 and 8.

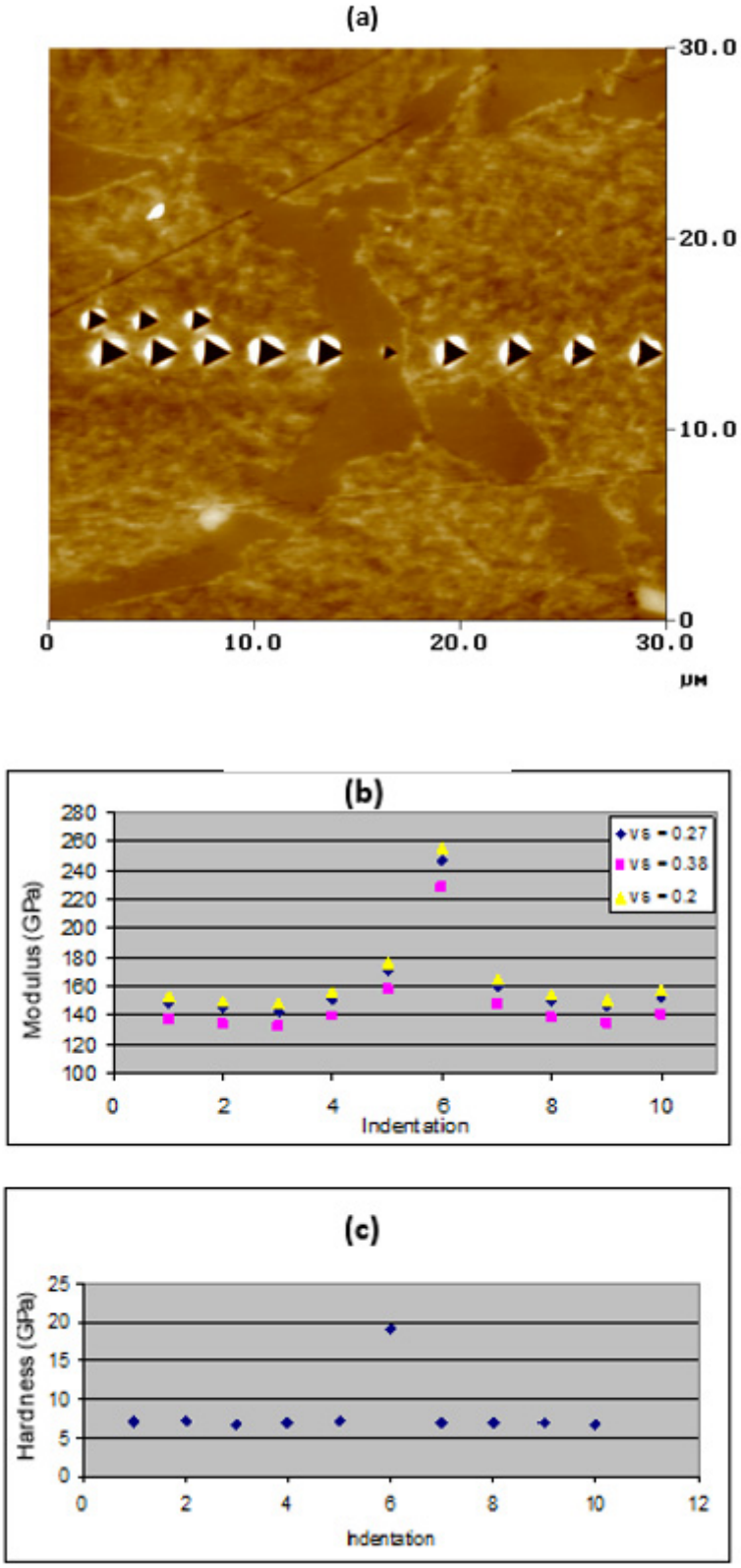

Figure 10. Data for (**b**) modulus and (**c**) hardness of Nb_{ss} and Nb_5Si_3 in NV1-AC for (**a**) a nano-indentation line scan crossing a Nb_5Si_3 grain located between two Nb_{ss} grains. The three smaller nano-indentations on the left-hand side of (**a**) above the row of lager nano-indentations were produced with a load of 4000 µN.

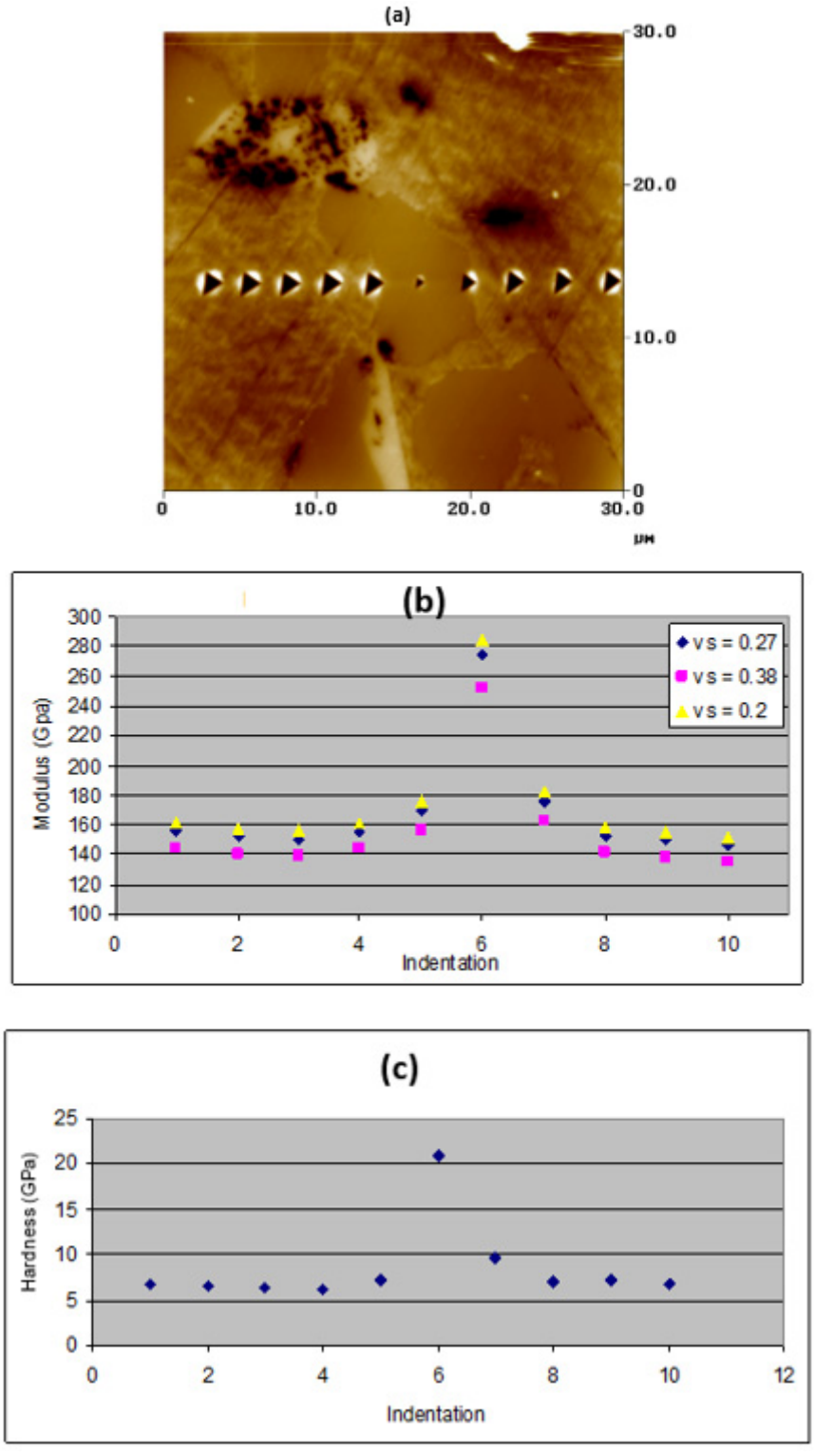

Figure 11. Data for (**b**) modulus and (**c**) hardness of Nb_{ss} and Nb_5Si_3 in NV1-HT for (**a**) a nanoindentation line scan crossing a Nb_5Si_3 grain located between two Nb_{ss} grains.

Table 7. Average modulus and hardness results from tests performed with a 7000 μN load showing the changes of property with regard to the distance from the Nb_5Si_3; data for as-cast (AC) and heat-treated (HT) conditions.

Condition and Property (GPa)	Average Value for Nb_5Si_3	Distance from Nb_5Si_3			Average Value for Nb_{ss}
		0–5 μm	5–10 μm	+10 μm	
AC—modulus	**230.7**	144.5	136.5	138.8	139.9
HT—modulus	285.1	146.1	137.7	140.5	141.4
AC—hardness	17.02	7.1	7.0	7.0	7.04
HT—hardness	20.93	7.2	6.8	6.9	6.97

Table 8. Average nano-hardness data (GPa) and Vickers hardness (HV) values for Nb_{ss} and Nb_5Si_3.

Condition	Nb_{ss}		Nb_5Si_3	
	(GPa)	HV	(GPa)	HV
AC	7.04	718	17.02	1737
HT	6.97	711	20.93	2136

5. Discussion

5.1. Microstructures

The solidification of NV1-AC started with the Nb_{ss} as the primary phase. The formation of Nb_3Si was suppressed owing to the destabilising effect of Sn [39] or Al [36] on Nb_3Si in the presence of Ti, and the destabilising effect of Sn on Nb_3Si when it is in synergy with Hf or Al (alloys EZ1 and EZ7 in [28]) or in synergy with Hf and Al or Cr (alloys EZ3 and EZ4 in [28]), even though Nb_3Si can form when Hf is in synergy with Cr in the absence of Ti (alloy YG1 in [40]) or in synergy with Ti in the absence of Al, Cr, or Sn ([33] and alloy YG3 in [40]). Furthermore, V forms cubic V_3Si (cP8, A15, and prototype Cr_3Si) [24] that is isomorphous with Nb_3Sn and A15-Nb_3Si [41], and thus the presence of V in NV1 would be expected to destabilise on tP32 Nb_3Si. No A15-Nb_3X (X = Al,Si,Sn) was observed in NV1 owing to the low Sn concentration [14].

When the stable (tP32) Nb_3Si is suppressed in the Nb-Si binary under RS conditions, the Nb_{ss} + Nb_3Si stable eutectic is replaced by the Nb_{ss} + βNb_5Si_3 metastable eutectic with Si content about 20 at.% [42]. However, the latter concentration depends on the version of the Nb-Si binary used to define the composition of the stable eutectic [43], which can be in the range 15.3 to 18.7 at.% Si [17,43]. In RM(Nb)ICs, the eutectics with Nb_{ss} and Nb_5Si_3 have <Si> in the range 21.6 to 24.3 at.% (<Si> = Al + Ge + Si + Sn, [43]). In the case of NV1-AC, the average <Si> content of the lamellar micro-structure was 25.1 at.% (Table 2) or 24.9 at.% for the five lamellar microstructures shown in Figure 3.

In RM(Nb)ICs, the type of Nb_5Si_3 (meaning tetragonal α or β) and the completion or not of the transformation $\beta Nb_5Si_3 \rightarrow \alpha Nb_5Si_3$ depends on the size of the as-cast button/ingot, meaning in "large" button/ingots the above transformation can occur during solid state cooling of the as-cast alloy (see Table A3 in [28] and alloy CM1 in [27]), the method of casting (see alloy CM1 in [27]) and the DS conditions ([33] and alloy CM1 in [27]), the heat treatment temperature and duration of treatment (see Table A3 in [28]), and the alloying addition(s). For example, the 5-3 silicides of Cr and V are isomorphous with βNb_5Si_3 [24]; the addition of Sn in RM(Nb)ICs with/without Ti quickens but does not lead to the completion of the above transformation in as-cast large button/ingots [28,39], and the same is the case when Hf is in synergy with Al, Cr, and Ti in RM(Nb)ICs (see Table A3 in [28]). On the other hand, the synergy of Al with Ti favours the βNb_5Si_3 in as-cast large button/ingots, and the above transformation is completed after prolonged heat treatment at 1500 °C [36], whereas when Al is in synergy with Cr and Ti, said transformation is not completed for the same heat treatment conditions (see Table A3 in [28]). When tetragonal Nb_3Si is formed, the αNb_5Si_3 forms from the eutectoid transformation $Nb_3Si \rightarrow Nb + \alpha Nb_5Si_3$, which is very sluggish.

In binary Nb-Si alloys, the hexagonal γNb_5Si_3 is metastable and can be stabilised by interstitials [2]. In RM(Nb)ICs, the formation/stability of γNb_5Si_3 depends (a) on the Hf and Ti concentrations and the Nb/(Ti + Hf) ratio in Sn-free RM(Nb)ICs [33]; (b) on the synergy of Hf with other alloying additions, in particular Al and Sn, in Ti-free RM(Nb)ICs (e.g., alloy EZ4 in [28]); and (c) on the synergy of Hf and Sn with Al and/or Cr in Ti-containing RM(Nb)ICs [29]. Nb_5Si_3 with Nb/(Ti + Hf) < 1 is most likely to have a hexagonal structure in RM(Nb)ICs with small Nb/(Ti + Hf) ratio, and this likelihood increases as the Nb/(Ti + Hf) ratio gets smaller [33]. In the alloy NV1-AC, the EPMA analyses confirmed the presence of Nb_5Si_3, which according to XRD had tetragonal (αNb_5Si_3) and hexagonal structures, and the EPMA analysis data indicated that the ratio Nb/(Ti + Hf) was less or greater than one (Figures 2b and 3, Table 2). The αNb_5Si_3 and γNb_5Si_3 were also reported in Sn-free DS Nb-Ti-Si-Hf RM(Nb)ICs with 0.85 < Nb/(Ti + Hf) < 1.95 [33]. The alloy NV1-AC had Nb/(Ti + Hf) = 1.81.

Figure 3 shows that the lamellar microstructure was "connected" with ("grew" from) Nb_5Si_3 that had Nb/(Ti + Hf) less than one, i.e., hexagonal γNb_5Si_3. Figures 2b and 3d provide unconvincing evidence that a lamellar microstructure with brighter contrast, similar to that of hexagonal γNb_5Si_3, is also associated with Nb_5Si_3 that has Nb/(Ti + Hf) greater than one, i.e., tetragonal αNb_5Si_3 (see brighter contrast area between silicides 2 and 3 and above and to the right of silicide 3 in Figure 2b, owing to the partitioning of Hf and Ti in Nb_5Si_3, and the slightly darker contrast area in the silicide 6 in Figure 3c from which "grew" the lamellar microstructure between silicides 6 and 7). Note that the lamellar microstructure was not stable in NV1-HT. Was the lamellar microstructure that was observed in NV1-AC a eutectic, a eutectoid, or a combination of eutectic and eutectoid microstructure?

Bewlay et al. [33] studied the microstructures of DS RM(Nb)ICs (nominal compositions, at.%) Nb-33Ti-16Si-12.5Hf (Nb/(Ti + Hf) = 0.84), Nb-33Ti-16Si-7.5Hf (Nb/(Ti + Hf) = 1.1), and Nb-21Ti-16Si-12.5Hf (Nb/(Ti + Hf) = 1.48). In the alloy with the lowest Nb/(Ti + Hf) ratio, they reported (i) that $(Nb + \gamma Nb_5Si_3)_{eutectic}$ formed via the solidification route L→tP32 Nb_3Si→tP32 Nb_3Si + Nb→$(\gamma Nb_5Si_3 + Nb)_{eutectic}$, i.e., from the tetragonal Nb_3Si, and (ii) that $(Nb + \gamma Nb_5Si_3)_{eutectoid}$ formed after heat treatment at 1200 °C for 24 h where the prior Nb_3Si + Nb eutectic microstructure was still present and the eutectoid γNb_5Si_3 grew epitaxially off the fine-scale eutectic γNb_5Si_3. The partitioning of Hf and Ti in Nb_5Si_3 played a key role in both transformations. No $(Nb + \gamma Nb_5Si_3)_{eutectic}$ was observed in the alloys with a higher Nb/(Ti + Hf) ratio, but the $(Nb + \gamma Nb_5Si_3)_{eutectoid}$ formed after heat treatment at 1200 °C for 50 h in all the Nb-Ti-Si-Hf RM(Nb)ICs with 0.85 < Nb/(Ti + Hf) < 1.95. In the RM(Nb)IC Nb-21Ti-16Si-7.5Hf (Nb/(Ti + Hf) = 1.95), only a small volume fraction of $(Nb + \gamma Nb_5Si_3)_{eutectic}$ formed, and this was observed only in the regions that were rich in Ti, owing to the partitioning of Ti, where the ratio Nb/(Ti + Hf) was greater than 1.5. It should be noted that in NV1-AC the areas of the alloy where the lamellar microstructure was observed had average Nb/(Ti + Hf) = 1.62 and that the Nb/(Ti + Hf) ratio of NV1-AC and NV1-HT was 1.81 and 1.92, respectively.

Likewise, Nb_3Si was present in the as-cast (arc-melted) alloy YG3 (Nb-24Ti-18Si-5Hf [40]) where Nb + Nb_3Si eutectic was formed as well as a fine-scale eutectic of Nb_{ss} and Nb_5Si_3 in which Ti-rich areas were noticeable and with average composition 34.3Nb-36.8Ti-21Si-7.9Hf (Hf and Si content essentially the same as in the lamellar microstructure in NV1-AC). Evidence for γNb_5Si_3 in the as-cast alloy YG3 was weak. However, after heat treatment (1500 °C/100 h), Hf-rich Nb_5Si_3 with Nb/(Ti + Hf) = 0.74, i.e., hexagonal Nb_5Si_3, formed, and the Nb_3Si was also present. Furthermore, in the as-cast large button/ingot of the RM(Nb)IC Nb-24Ti-18Si-5Al-5Hf-5Sn, the $(Nb + \gamma Nb_5Si_3)_{eutectic}$ with <Si> =23.2 at.% formed only in the bulk, and Hf-rich Nb_5Si_3 (<Si> = 38 at.%) grew from Nb_5Si_3 (<Si> = 36.9 at.%) in the bottom of the ingot. The eutectic γNb_5Si_3 had Nb/(Ti + Hf) = 0.7 and <Si> = 38.5 at.% [29].

Given the above data from Bewlay et. al. [33] and our research group [28,29,40], the analysis data for NV1-AC and NV1-HT, the types of Nb_5Si_3 in NV1-AC and NV1-HT, the

absence of tP32 Nb_3Si and A15-Nb_3Sn in both conditions, and the characteristic features of the lamellar microstructures in NV1-AC (Figure 2a,b and Figure 3 and Table 2), it is suggested that the solidification paths in NV1-AC were (i) L→L + Nb_{ss}→Nb_{ss} + βNb_5Si_3 →Nb_{ss} + αNb_5Si_3, where the βNb_5Si_3→αNb_5Si_3 transformation occurred during solid state cooling (parts of Figure 2b), or (ii) L→L + Nb_{ss}→Nb_{ss} + βNb_5Si_3→ Nb_{ss} + αNb_5Si_3 + γNb_5Si_3 (with the formation of γNb_5Si_3 attributed to the partitioning of solutes, parts of Figure 2b), or (iii) L→L + Nb_{ss}→ Nb_{ss} + βNb_5Si_3→Nb_{ss} + αNb_5Si_3 + γNb_5Si_3→ Nb_{ss} + αNb_5Si_3 + γNb_5Si_3 + (Nb + γNb_5Si_3)$_{eutectic}$ (Figures 2a and 3 and part of Figure 2b) with the possibility of some (Nb + γNb_5Si_3)$_{eutectoid}$ forming during solid state cooling. Because of this uncertainty about the presence of (Nb + γNb_5Si_3)$_{eutectoid}$ in NV1-AC, the lamellar microstructure is not designated eutectic in the Table 2.

In NV1-AC, owing to their average chemical compositions, both the Ti-, Cr-, and V-rich Nb_{ss} and the lamellar microstructure had a composition that corresponds to RCCAs (i.e., they were "RCCA phases") but not the Nb_{ss} and Ti-rich Nb_{ss}. In other words, because of the solidification conditions and the partitioning of solutes' "conventional" phases, i.e., Nb_{ss} and Ti-rich Nb_{ss}, and "RCCA phases" co-existed in the aforementioned solidification paths. However, the latter phases were not stable (not observed in NV1-HT). A similar co-existence of "conventional" and RHEA alloys was reported in the arc-melted RHEA of nominal composition (at.%) 13Nb-24Ti-24Si-35Al-4Hf [44]. The formation of bcc Nb_{ss} and eutectics with Nb_{ss} and Nb_5Si_3 that satisfy the "standard definition" of HEAs is not rare in RM(Nb)ICs [17,43].

In NV1-AC, the average Si solubility in Nb_{ss} and in the Ti-rich Nb_{ss} was similar to that reported (i) for alloys of the Nb-Ti-Si and Nb-Hf-Si systems by Bewlay et al. [45,46], (ii) for the Nb-24Ti-18Si-5Hf alloy (YG3 in [40]), and (iii) for alloys of the Nb-Ti-Si-Cr-Al system such as KZ3, KZ4, KZ5, and KZ7 (often referred to by our group as the KZ series of alloys, see [35,36]), but it was higher than that in the Nb_{ss} in the Nb-24Ti-18Si-5Sn (alloy NV6 in [39]) and in the alloy KZ2 with higher Cr concentration [36]. The increase in the solubility of Si in the solid solution with increasing Hf concentration is supported by the work of Bewlay et al. [31]. The solubility of Si in the Nb_{ss} was not sensitive to the V concentration, which is in agreement with [47].

The average Ti concentrations in Nb_{ss} and in the Ti-rich Nb_{ss} were lower than those reported in [35,45] for alloys of the Nb-Ti-Si system, for alloys of the Nb-Ti-Si-Al-Cr system [35,36], for the alloy YG3 [40], and for the alloy NV6 [39]. This difference was more significant for the Nb_{ss}. The presence of V led to a further increase in the average Ti concentration in parts of the Nb_{ss} where the solubilities of Cr, V, and Hf had also increased. In some of these parts, the solubility of Ti was similar to that reported for alloys of the Nb-Ti-Si and Nb-Ti-Si-Cr-Al systems [35,36,45] and alloy NV6 [39]. The increase in the solid solubilities of Al, Cr, and Hf in the Nb_{ss} with increased Ti concentration is in agreement with the results for the KZ series of alloys [35,36]; the alloys JG2, JG3, JG4, and JG6 with/without Hf (JG series of alloys) [6,48,49]; and the alloy YG3 [40]. It was concluded (i) that the solubilities of Al, Cr, and Hf in the Nb_{ss} increased with increasing Ti concentration in agreement with previous research and (ii) that the solubility of V in the Nb_{ss} also increased with the Ti content.

In NV1-AC, the solubility range of Hf in the Hf rich Nb_5Si_3 was in agreement with the data in [32,46,50] but was significantly higher than the data in [49] for the Hf-containing and Hf-and-Sn-containing alloys JG4 and JG6, respectively. Furthermore, the solubility of Hf in the Ti-rich Nb_5Si_3 in NV1-AC was in agreement with data for the Hf-rich Nb_5Si_3 in JG4 and JG6 [49]. The solubility of Sn in Nb_5Si_3 was significantly lower than the data for alloys JG6 [49] and NV6 [39], and the same was the case regarding the solubility of Cr, compared to the KZ series of alloys [35,36] and the JG series of alloys [48,49]. The solubility of V in Nb_5Si_3 did not depend on the Ti or Hf solubilities and was significantly higher than the solubility of Mo [48] but significantly lower than the solubility of Ta in Nb_5Si_3 [36]. However, the highest concentration values for V in Nb_5Si_3 were significantly lower than the data reported in [47]. Comparison of the solubilities of V in the Nb_{ss} and

Nb_5Si_3 would suggest that V predominantly partitions to the former phase, which is also supported by the data for the aforementioned phases in NV1-HT and is in agreement with [47]. Finally, the solubility of Al in Nb_5Si_3 was the same as for the KZ and JG series of alloys [35,36,48,49].

The average Si and Sn concentrations of the lamellar microstructure in NV1-AC were higher and lower than the corresponding values for the Nb_{ss} + Nb_5Si_3 eutectics in NV9 and NV6 [39], respectively; within the range of the Si concentrations suggested for the Nb_{ss} + Nb_5Si_3 eutectic in the Nb-V-Si system [47]; and higher than that of the Nb-Si eutectic in the binary system [51] and the eutectics in JG series of alloys [6]. The average Hf concentration of the eutectic was the same as for the Nb_{ss} and Nb_5Si_3 eutectic in the alloy YG3 [40], but the Si concentration was lower.

The suppression of Nb_3Si resulted to equilibrium between Nb_{ss} and γNb_5Si_3 in the bulk and between Nb_{ss} and αNb_5Si_3 in the near-the-surface areas of NV1-HT, according to the XRD and EPMA data (Tables 2 and 3 and Figure 1b). In NV1-HT, the Si solubility in Nb_{ss} was reduced compared with NV1-AC but was still higher compared with the heat-treated KZ series of alloys [35,36], the JG series of alloys [49], and the alloy NV6 [39]. Compared with NV1-AC, the solubility of V in Nb_{ss} and Nb_5Si_3 was reduced; the solubility of Cr in Nb_5Si_3 was increased; and the average solubility of Hf in Nb_5Si_3 was the same as in the Hf-rich Nb_5Si_3 in NV1-AC but with a significantly lower Ti concentration in the Nb_5Si_3.

The lamellar microstructure was not observed in NV1-HT. Given that the prior eutectic microstructure was stable in heat-treated Nb-V-Si alloys [47] and not completely eliminated in NV6-HT [39] and that the prior eutectic microstructure was not observed in the heat-treated KZ and JG series of alloys [35,36,48,49], it is suggested that it is the synergy of Cr and Al that has the strong detrimental effect on the stability of Nb_{ss} + Nb_5Si_3 lamellar microstructures. The formation of HfO_2 in the as-cast alloy and of TiN in the near-the-surface areas of the heat-treated alloy demonstrated the sensitivity of NV1 to interstitial contamination, which was also confirmed by the oxidation results.

5.2. Oxidation

Compared with the alloy ZX7 [14], which had the same Sn concentration as NV1 but which was V-free, the addition of the latter element and Hf, and the lowering of the Si concentration in NV1, had an effect on (i) the chemical composition of the scale, (ii) the thickness of the scale, (iii) the enrichment of the subscale area of the substrate with Sn, and (iv) the formation of Sn rich layer at the scale/substrate interface. The oxides in the scale of NV1 at 900 °C were the same as those reported for Sn-free and for Sn-containing RM(Nb)ICs [13–15,17–19]. The oxygen content of the scale of NV1 was in agreement with the Si-rich oxide in the alloy ZX7 and (the richer in Sn) alloy ZX8 and the Nb-and-Ti-rich oxide in the alloy ZX8 [14,15]. However, the Cr and Sn concentrations in the scale of NV1 were remarkably low compared with the alloy ZX7 [14]. Additionally, in the scale, the V content was markedly low but hafnia was present in it (Table 5). The scale of NV1 was thinner than that of ZX7 ($\leq$20 μm and 40 μm, respectively), but unlike the latter its thickness was not uniform.

Contrary to the alloy ZX7 [14], in which formation of an Sn-rich layer at the scale/substrate interface was not observed at 800 °C, a thin Sn-rich layer was observed in the alloy NV1 at 800 °C, the thickness of which increased at 900 °C (Figure 7b, Figure 8, and Figure 9), where it consisted of the Nb_3Sn and Nb_6Sn_5 compounds. Note (i) that these two compounds can be at equilibrium below about 916 °C [24], (ii) that the melting temperature of Nb_6Sn_5 is about 916 °C, (iii) that the oxidation of NV1 at T $\geq$ 1000 °C was catastrophic (results not reported in this study), and (iv) that A15-Nb_3X (X = Al,Si,Sn) was not observed in NV1-AC and was not stable in NV1-HT. In other words, in the alloy NV1, similarly to the (richer in Sn) alloy ZX8 [15], an Sn-rich layer formed at said interface. Of the two compounds that made different parts of this layer (Figure 9), the Nb_3Sn has been reported in richer in Si and Sn but V-free RM(Nb)ICs with/without Hf, in which the compounds Nb_5Sn_2Si and $NbSn_2$ also have been observed [13,15], but not the Nb_6Sn_5. Remarkably, in NV1, the latter

compound was not contaminated with oxygen compared with the Nb_3Sn, the contamination of which was more severe than in the alloys JG6 and ZX8 [13,15]. Furthermore, in NV1, both the Nb_3Sn and Nb_6Sn_5 were Cr free, and even though their V concentration was very low, it was double in the former than in the latter compound.

The consumption of solute additions in NV1 for the formation of (a) the scale, in particular Al, Hf, Si, and Ti; and (b) the Sn-rich layer, especially Al, Si, Sn, and Ti, resulted in the bulk composition at 800 °C being poorer in these elements compared with NV1-AC. Composition changes from the bulk to the surface of NV1 at 800 °C were expected owing (i) to the tendency of Al, Cr, Si, Sn, and Ti to segregate to the surface [14] and (ii) the presence of Ti-rich Nb_5Si_3, Ti nitride, and hafnia in the near surface areas of NV1-HT (Table 3). In Figure 7b, the Nb_5Si_3 grains shown with the analysis numbers 1 and 2 were not contaminated with oxygen, and their composition corresponded to hexagonal γNb_5Si_3 ((Nb/(Ti + Hf) equal to 0.95 and 0.78, respectively, analysis number 1: 29.1Nb-20.1Ti-35.1Si-3.5Al-0Cr-10.6Hf-0Sn-1.6V and analysis number 2: 25.8Nb-21.2Ti-35.6Si-3.2Al-0.5Cr-11.8Hf-0Sn-1.9V), whereas the Nb_5Si_3 grains shown with the analysis numbers 3 and 11 were also hexagonal γNb_5Si_3 ((Nb/(Ti + Hf) equal to 0.94 and 0.8, respectively) and contaminated, the latter more severely owing to its proximity with the scale/substrate interface (analysis number 3: 26.5Nb-18.6Ti-33.4Si-3.1Al-0.4Cr-9.7Hf-0.3Sn-1.3V-6.7O, analysis number 11:22.2Nb-18.3Ti-29.5Si-2.6Al-0.4Cr-9.3Hf-0.3Sn-1.5V-15.9O). Further in from the scale/substrate interface and toward the bulk, the contamination of Nb_5Si_3 was reduced, and there was oxygen-free (i.e., non-contaminated) Nb_5Si_3 in the bulk (Table 5). All the Nb_{ss} grains shown with the analysis numbers 4 to 9 in Figure 7b were contaminated with oxygen, and the chemical composition of the grains shown with the numbers 4 to 8 was similar (average composition 35.4Nb-14.8Ti-1.4Si-2.7Al-1.4Cr-2.6Hf-1.5Sn-2.9V-37.3O), whereas the composition of grain 9, below the Sn-rich layer, was slightly richer in Ti and V (31.4Nb-17.8Ti-1.1Si-3.5Al-2.1Cr-2.9Hf-1.8Sn-4V-35.4O). The contamination of the microstructure with oxygen from the scale/substrate interface to the bulk of NV1 followed the Ti-rich and Ti-, Cr-, and V-rich areas of Nb_{ss} grains on either side of Nb_5Si_3 grains (Figures 7b–d and 9) and the Nb_{ss} in the lamellar microstructure (Figure 7c,d). In the latter, the more severe contamination of the Nb_{ss} resulted in "disintegration" (break-up and degeneration) of the lamellae (Figure 7c,d).

In spite of the fact that its microstructure was contaminated with oxygen from the scale/substrate interface to the bulk, and its very high vol.% Nb_{ss}, which played the key role in the contamination, the oxidation behaviour of the alloy NV1 in the pest regime was remarkable. Indeed, compared with other Sn-containing alloys with the same (alloy ZX7 [14]) or higher Sn content (alloys ZX8 [15] and JG6 [13] and the NV series alloys in Table 4) and the MASC alloy, the alloy NV1 (a) did not suffer from catastrophic pest oxidation, (b) had a mass change at 800 °C significantly lower than those of the alloys ZX7 and ZX8 (about 60 and 40 mg/cm^2, respectively [15]), (c) had oxidation rate constants at 800 °C similar to those of the alloys ZX7 [14] and JG6 [13], and (d) had less mass change at 900 °C than all the other alloys in the Table 4, including the alloy NV5 that had the lowest vol.% Nb_{ss} (1.9%). However, compared with the alloy NV5, at 800 °C, the parabolic rate constant of NV1 was two orders of magnitude higher and its mass change 14 times higher.

Concerning the oxidation of RM(Nb)ICs in the pest regime, the results of this work (a) underpinned the benefits of alloying with Sn, (b) emphasised the key role of Nb_{ss} for the contamination of the alloy, (c) provided new data that show that the chemical composition of Nb_{ss} is as important as its vol.% for the oxidation behaviour of RM(Nb)ICs, and (d) showed that a 2 at.% Sn addition might be good enough for oxidation resistance purposes, depending on the other alloying additions and their concentrations. It is suggested that (a) to (d) are relevant to other multiphase metallic UHTMs with Nb addition, namely, RHEAs and RCCAs [10,11].

How does the isothermal oxidation of NV1 in the pest regime temperatures compare with the RCCAs in the review in [52]? At 700 °C, the mass change of NV1 (3.5 mg/cm^2) was lower than those of the single phase bcc solid solution RRCAs $Al_{0.3}$HfNbTaTiZr, $Al_{0.5}$HfNbTaTiZr, $Al_{0.75}$HfNbTaTiZr, AlHfNbTaTiZr, and HfNbTaTiZr (14, 14, 11, 10, and

55 mg/cm^2 after 100 h, respectively). At 900 °C, the mass change of NV1 (30 mg/cm^2) was lower than HfNbTaTiZr (54 mg/cm^2), the same as $Al_{0.3}$HfNbTaTiZr, but higher than $Al_{0.5}$HfNbTaTiZr (18 mg/cm^2), $Al_{0.75}$HfNbTaTiZr (17 mg/cm^2), and AlHfNbTaTiZr (16 mg/cm^2). In other words, at 700 °C, the mass change of the alloy NV1 was less than all the aforementioned richer in Al, Ti, and Hf RCCAs, whereas, at 900 °C, the mass gain of the latter was less than NV1 only when their Al, Hf, or Ti concentrations were in the ranges 9.1 < Al < 16.7 at.% and 16.7 < Hf or Ti < 18.9 at.%.

5.3. Hardness and Nanoindentation

In nanoindentation, from the unloading curve, the stiffness, S, of the phase can be measured. The stiffness is correlated with the reduced modulus E_r with the equation:

$$S = \frac{dP}{dh} = \frac{2}{\sqrt{\pi}} E_r \sqrt{A}$$

where P is the load, h is displacement, and A is the projected surface area of the indentation. The reduced modulus E_r accounts for the effects of a non-rigid indenter during loading and is given by the equation:

$$\frac{1}{E_r} = \frac{(1-\nu_s{}^2)}{E_s} + \frac{(1-\nu_i{}^2)}{E_i}$$

where E_s and ν_s are the Young's modulus and Poisson's ratio of the phase, respectively, and E_i, ν_i are the parameters for the indenter [53]. A rearrangement of the last equation gives the actual modulus, E_s, of the phase as:

$$E_s = \frac{E_r E_i (1-\nu_s{}^2)}{E_i - E_r(1-\nu_i{}^2)}$$

The values of E_i and ν_i were specified in the TriboScope manual [34] as 1140 GPa and 0.07, respectively. The E_s was calculated for three different values of ν_s, namely, 0.38, 0.27, and 0.2 [54,55] (Figures 10b and 11b). The average E_s values of the Nb_{ss} and Nb_5Si_3 given in the Table 7 were from the E_s calculated with ν_s equal to 0.38 and 0.27, respectively.

The Young's modulus of the Nb_{ss} in NV1-HT (Table 7) was about 10 GPa higher than the average modulus of the Nb_{ss} in the heat-treated Sn-free alloys KZ5, KZ6, and KZ7 [56,57] (131.1 GPa, range 115.7 to 138.6 GPa) and about 8 GPa lower than the average modulus of the Nb_{ss} in the heat-treated Sn-free and Ge-containing alloys ZF4, ZF5, and ZF6 [58] (148.1 GPa, range 142.2 to 154 GPa), all calculated from nanoindentation data for the Nb_{ss} with ν_s = 0.38. Given that the aforementioned ZF series alloys were based on KZ series alloys with the addition of Ge, the data would suggest (a) that the alloying of the Nb_{ss} with Ge or Sn increases the elastic modulus of Nb_{ss} and (b) that the addition of Ge has a stronger effect (plus 17 GPa) than that of Sn (plus 10 GPa). The increase in the modulus of the Nb_{ss} near the Nb_{ss}/Nb_5Si_3 interface in NV1-AC and NV1-HT should be noted in Table 7.

The Young's modulus of unalloyed (binary) Nb_5Si_3 decreases in the sequence $\alpha Nb_5Si_3 > \beta Nb_5Si_3 > \gamma Nb_5Si_3$ according to ab initio calculations (291, 268.9, and 188.5 GPa, respectively [54]; also see Table 3 in [59]). The alloying of Nb_5Si_3 with Ti increases the Young's modulus of $\alpha(Nb,Ti)_5Si_3$ and $\gamma(Nb,Ti)_5Si_3$ and decreases the modulus of $\beta(Nb,Ti)_5Si_3$ [54]. In RM(Nb)ICs, the Si can be substituted by other simple metal and metalloid element additions and Nb by other TM and RM additions (e.g., see Table 2 in [59]). To our knowledge, there is no data from experiments or calculations that shows how other (than Ti) alloying additions that substitute Nb or additions that substitute Si in Nb_5Si_3 affect the Young's modulus of the silicide.

The average E_s of the alloyed Nb_5Si_3 in NV1-HT (285.1, Table 7) was lower than the moduli of $\alpha(Nb,Ti)_5Si_3$ reported in [54] and of αNb_5Si_3 reported in [60] and [61] (314.3 and 325 GPa, respectively), and it was essentially the same as that of the alloyed $\alpha(Nb)_5(Si)_3$

in KZ7-HT (283.8 GPa, calculated with ν_s = 0.27 [56]; the Nb and Si are in parentheses to indicate that they are substituted by other elements in the 5-3 silicide), which, however, was lower than the calculated moduli of $\alpha(Nb,Ti)_5Si_3$ [54]. It should be noted that the silicides in the alloys KZ7 and NV1 were $(Nb,Ti)_5(Si,Al)_3$ and $(Nb,Cr,Hf,Ti,V)_5(Si,Al,Sn)_3$, respectively. Furthermore, the average E_s of the $(Nb)_5(Si)_3$ in NV1-AC was significantly lower (230.7 GPa, Table 7) than said value in NV1-HT and closer to the moduli of hexagonal $\gamma(Nb,Ti)_5Si_3$ and alloyed hexagonal $(Ti)_5Si_3$ [54]. This difference (i) could be attributed to the fact that the nanoindentation measurements could not differentiate between the three different types of Nb_5Si_3 in the alloy (Table 2, Figure 1a) but also (ii) could indicate that in NV1-AC, where in the microstructure shown in Figure 2b the silicide is αNb_5Si_3 ((Nb/(Ti+Hf) > 1, see Section 4.1 and 5.1), the alloying of $\alpha(Nb,Ti,Hf,Cr,V)_5(Si,Al,Sn)_3$ caused significant reduction in the Young's modulus, whereas in NV1-HT, where the silicide was $\gamma(Nb,Ti,Hf,Cr,V)_5(Si,Al,Sn)_3$ ((Nb/(Ti+Hf) < 1, Table 2, Figure 2d), the alloying increased notably the Young's modulus.

The hardness of Nb_{ss} and Nb_5Si_3 in RM(Nb)ICs that is measured using nanoindentation (nH) can be different from the microhardness (μH). The average correction factors derived from the data for the Nb_{ss} and Nb_5Si_3 in heat-treated KZ series alloys [56–58] and NV1-HT was 0.7357 for the former and 0.6395 for the latter; in other words, $\mu H_{Nbss} = 0.7357 \times nH_{Nbss}$ and $\mu H_{Nb5Si3} = 0.6395 \times nH_{Nb5Si3}$. For the particular case of KZ7-HT, where only the $\alpha(Nb,Ti)_5(Si,Al)_3$ was present [36], the correction factor was 0.6275. Furthermore, the microhardness of binary αNb_5Si_3 and alloyed $\alpha(Nb)_5(Si)_3$ was higher than that of the binary βNb_5Si_3 and alloyed $\beta(Nb)_5(Si)_3$ (see Table 4 in [59]). The microhardness of Nb_{ss} in NV1 calculated from the nanoindentation data and the aforementioned correction factor was 528.2 and 523.1 HV for NV1-AC and NV1-HT, respectively, which was in good agreement with the measured average values, particularly the former. The microhardness of Nb_5Si_3 was 1090 and 1340.3 HV for NV1-AC and NV1-HT, respectively. The former value was lower than the hardness of Nb_5Si_3 in the alloy NV6-HT [39] and in other Ti-containing RM(Nb)ICs (see the Figure 3 in [59]) but close to the hardness of $(Nb,Ti,Hf,Cr)_5(Si,Al,Sn)_3$ (1100 HV, [29]).

In Table 9, the measured average hardness of NV1 with the calculated hardness is compared. The calculations used the data for vol.% of phases in Table 1 (the vol.% hafnia is the balance), the microhardness values of the Nb_{ss} and Nb_5Si_3 calculated from the nanoindentation data, and 918 HV, the microhardness of hafnia. The calculated hardness is given for the law of mixtures, a Pythagorean-type addition rule, an inverse-type addition rule [28,39] and a cube-type addition rule $(HV)^3 = \Sigma[V_i(HV)_i]^3$ where V_i is the volume fraction of phase i. The calculated values from the Pythagorean-type addition and the cube-type addition are closest to the measured values for NV1-AC and NV1-HT, respectively. The measured hardness of NV1-HT was lower than that of NV1-AC owing to the higher vol.% Nb_{ss} and the lower vol.% of Nb_5Si_3 compared with NV1-AC.

Table 9. Measured and calculated Vickers hardness of NV1.

Alloy and Condition	Measured *	Calculated +			
		A	B	C	D
NV1-AC	475	639.2	459.4	585.9	432
NV1-HT	454	670.5	480	640.8	442.5

* Average value from Table 1, + see text. A = law of mixtures. B = Pythagorean-type addition. C = inverse-type addition. D = cube-type addition.

How does the room temperature hardness of NV1-AC (475 HV, Table 1) and of the bcc Nb_{ss} in the cast alloy (531 HV or 528 HV; the latter value was calculated from nanoindentation hardness, see above) compare with that of single-phase bcc solid solution as-cast RCCAs? Table 3 in [52] reports the hardness of 12 as-cast RCCAs. Five RCCAs had a hardness in the range of 298 to 454 HV, namely, (in increasing hardness) the alloys NbTaTiV, HfNbTaTiZr, MoNbTaTiV, NbTaTiVW, and MoNbTaW, whereas the hardness of six RCCAs, namely, NbTaVW, MoNbTaV, HfMoNbTaTiZr, MoNbTaVW, HfMoTaTiZr,

and HfNbTaTiVZr were in the range 493 to 558 HV, and the hardness of CrMoNBTaVW was 705 HV. In other words, the hardness of NV1-AC was higher than that of the first five aforementioned RCCAs, and the hardness of the Nb_{ss} in NV1-AC was lower only than four of the above mentioned RCCAs, namely, the alloys CrMoNbTaVW, HfNbTaTiVZr, HfMoTaTiZr, and MoNbTaVW. Note that the mass change of NV1 at 700 and 900 °C was also better than that of HfNbTaTiZr (see previous section).

The room temperature yield stress of NV1-AC calculated from hardness was 1552.7 MPa, and the specific yield stress was 210.4 $MPacm^3g^{-1}$. The yield stress of NV1-AC was higher and lower than the yield stress of two RCCAs with a two-phase microstructure (bcc solid solution + M_5Si_3 silicide)—the $HfNbSi_{0.5}TiV$ (1399 MPa) and $HfMo_{0.5}NbSi_{0.3}TiV_{0.5}$ (1617 MPa)—whereas, the specific yield stress of NV1-AC was higher than both RCCAs (179.8 and 191.1 $MPacm^3g^{-1}$, respectively) [52]. Furthermore, the room temperature specific yield stress of NV1-AC was higher than most of the RCCAs reviewed in [52] (see Figure 6b and data in Table 2 in the ref. [52]).

5.4. Comparison with NICE

In Section 2, where the alloy design/selection was briefly discussed, the property goal and the constraints of the design were given together with the predicted values according to NICE. The latter overestimated MACSi (3.7 versus 3.1 at.%) and the mass change at 800 °C (14.8 versus 10 mg/cm^2), underestimated the vol.% of Nb_{ss} (75.5 versus 81 at.%), and predicted correctly the stable phases (meaning the Nb_{ss} and Nb_5Si_3 and the absence of Nb_3Si and A15-Nb_3X) and the room temperature yield stress from hardness. Given the uncertainties in the design of metallic UHTMs and RM(Nb)ICs [10,11,17], the agreement of NICE with the experimental results was satisfactory.

6. Conclusions

We studied the microstructure, isothermal oxidation, and hardness of the Nb-23Ti-5Si-5Al-5Hf-5V-2Cr-2Sn alloy and the hardness and Young's moduli of elasticity of its Nb_{ss} and Nb_5Si_3. There was macrosegregation of Ti and Si in the as-cast alloy. The microstructure consisted of the Nb_{ss}, αNb_5Si_3, γNb_5Si_3, and HfO_2 phases in the as-cast or heat-treated alloy plus TiN in the near-the-surface areas of the latter. The vol.% of Nb_{ss} was about 80%. There were Ti- and Ti-and-Hf-rich areas in the solid solution and 5-3 silicide, respectively, and a lamellar microstructure of these two phases in the cast alloy. The V partitioned to the Nb_{ss}, where its solubility increased with increasing Ti concentration. At 700, 800, and 900 °C, the alloy did not suffer from catastrophic pest oxidation; it followed parabolic oxidation kinetics in the former two temperatures and linear oxidation kinetics in the latter, where its mass change was the lowest compared with other Sn-containing alloys. A thin Sn-rich layer formed in the interface between the scale and the substrate, which consisted of the Nb_3Sn and Nb_6Sn_5 compounds at 900 °C. The latter compound was not contaminated with oxygen. Both the Nb_{ss} and Nb_5Si_3 were contaminated with oxygen (the former more severely than the latter). Furthermore, the bulk of the alloy was also contaminated with oxygen. However, in the bulk, some Nb_5Si_3 grains were not contaminated. The contamination of the microstructure with oxygen from the scale/substrate interface to the bulk followed the Ti- and Ti-, Cr-, and V-rich Nb_{ss} grains on either side of Nb_5Si_3 grains, and the Nb_{ss} in the lamellar microstructure, where the more severe contamination of the Nb_{ss} resulted in "disintegration" of the lamellae. The alloying of the Nb_{ss} with Sn increased its elastic modulus compared with Sn-free solid solutions. The hardness of the alloy and its Nb_{ss} and its specific room temperature strength compared favourably with many RCCAs. The research answered the three questions that motivated it, namely, that an RM(Nb)IC with very high vol.% Nb_{ss} (i) can have acceptable oxidation in the pest regime and that it (ii) will be contaminated with oxygen from the surface areas to its bulk. It also confirmed that in such an alloy both the αNb_5Si_3 and γNb_5Si_3 can be stable. The agreement of the predictions of the alloy design methodology NICE with the experimental results was satisfactory.

Author Contributions: Experimental work, N.V., P.K.; funding, P.T.; supervision, P.T.; resources, P.T.; formal analysis, N.V., P.K. and P.T.; draft preparation, N.V., P.K.; review, P.T.; final paper, P.T. All authors have read and agreed to the published version of the manuscript.

Funding: This research was funded by the EPSC (EP/H500405/1, EP/L026678/1).

Institutional Review Board Statement: Not applicable.

Informed Consent Statement: Not applicable.

Data Availability Statement: All the data for this paper is given in the paper, other data cannot be made available to the public.

Acknowledgments: Support of parts of this work by the University of Sheffield, Rolls-Royce Plc, EPSRC (EP/H500405/1, EP/L026678/1), and the University of Surrey is gratefully acknowledged.

Conflicts of Interest: The authors declare no conflict of interest.

Appendix A

Table 1. Nominal compositions (at.%) of reference alloys used in this work.

Alloy	Nb	Ti	Si	Al	Hf	Cr	Mo	Ta	W	Fe	Ge	Sn	Refs.
CM1	60.5	8.3	21.1	-	0.7	-	5.4	-	4	-	-	-	[27]
EZ1	72	-	18	-	5	-	-	-	-	-	-	5	[28]
EZ4	67	-	18	5	5	-	-	-	-	-	-	5	[28]
EZ5	43	24	18	5	5	-	-	-	-	-	-	5	[29]
EZ7	72	-	18	5	-	-	-	-	-	-	-	5	[28]
JG2 *	43	24	18	5	-	5	5	-	-	-	-	-	[48]
JG3 *	46	24	18	5	-	5	2	-	-	-	-	-	[48]
JG4 *	41	24	18	5	5	5	2	-	-	-	-	-	[49]
JG6 *	36	24	18	5	5	5	2	-	-	-	-	5	[49]
KZ2 **	46	24	18	4	-	8	-	-	-	-	-	-	[36]
KZ3 **	58	24	18	-	-	-	-	-	-	-	-	-	[34]
KZ4 **	53	24	18	-	-	5	-	-	-	-	-	-	[35]
KZ5 **	48	24	18	5	-	5	-	-	-	-	-	-	[35,36]
KZ7 **	53	24	18	5	-	-	-	-	-	-	-	-	[35,36]
MASC	47	25	16	2	8	2	-	-	-	-	-	-	[3]
NV3 +	48	24	18	-	-	5	-	-	-	5	-	-	[37]
NV4 +	30	45	15	-	-	-	-	-	-	5	-	5	[38]
NV5 +	43	24	18	-	-	5	-	-	-	5	-	5	[37]
NV6 +	53	24	18	-	-	-	-	-	-	-	-	5	[39]
NV8 +	48	24	18	-	-	-	-	-	-	5	-	5	[38]
NV9 +	77	-	18	-	-	-	-	-	-	-	-	5	[39]
YG1	72	-	18	-	5	5	-	-	-	-	-	-	[40]
YG3	53	24	18	-	5	-	-	-	-	-	-	-	[40]
YG4	72	-	18	-	5	-	2	3	-	-	-	-	[25]
YG5	70	-	20	-	5	-	-	-	5	-	-	-	[26]
YG6	72	-	20	-	-	-	5	-	3	-	-	-	[26]
YG8	67	-	20	-	5	-	5	-	3	-	-	-	[26]
ZF4 ++	48	24	18	-	-	5	-	-	-	-	5	-	[62]
ZF5 ++	48	24	18	5	-	-	-	-	-	-	5	-	[63]
ZF6 ++	43	24	18	5	-	5	-	-	-	-	5	-	[20]
ZX7	46	24	18	5	-	5	-	-	-	-	-	2	[14]
ZX8	43	24	18	5	-	5	-	-	-	-	-	5	[15]

* JG series alloys, + NV series alloys, ** KZ series alloys, and ++ ZF series alloys.

References

1. Mendiratta, M.G.; Dimiduk, D.M. Phase relations and transformation kinetics in the high Nb region of the Nb-Si system. *Scr. Metall. Mater.* **1991**, *25*, 237–242. [CrossRef]
2. Schlesinger, M.E.; Okamoto, H.; Gokhale, A.B.; Abbaschian, R. The Nb-Si (Niobium-Silicon) System. *J. Phase Equilibria* **1993**, *14*, 502–509. [CrossRef]
3. Bewlay, B.P.; Jackson, M.R. High-temperature in situ composites: Processing and Properties. In *Comprehensive Composite Materials*; Kelly, A., Zweben, C., Eds.; Chapter 3.22; Elsevier: Amsterdam, The Netherlands, 2003; pp. 579–615.
4. Jackson, M.R.; Bewlay, B.P.; Briant, C.L. Creep Resistant Nb-Silicide Based Two Phase Composites. US Patent 6,447,623, 10 September 2002.
5. Jackson, M.R.; Bewlay, B.P.; Zhao, J.-C. Niobium Silicide Based Composites Resistant to Low Temperature Pesting. US Patent 6,419,765, 16 July 2002.
6. Geng, J.; Tsakiropoulos, P. A study of the microstructures and oxidation of Nb-Si-Cr-Al-Mo in situ composites alloyed with Ti, Hf and Sn. *Intermetallics* **2007**, *15*, 382–395. [CrossRef]
7. Jackson, M.R. NbTiAlCrHf Alloy and Structures. US Patent 5,366,565, 22 November 1994.
8. Bewlay, B.P.; Jackson, M.R.; Gigliotti, M.F.X. Niobium Silicide High Temperature In-Situ Composites. In *Intermetallic Compounds, Principles and Practice*; Westbrook, J.H., Fleischer, R.L., Eds.; Wiley: Hoboken, NJ, USA, 2002; Volume 3, pp. 541–560.
9. Prokoshkin, D.A.; Vasil'eva, E.V. *Alloys of Niobium*; Samatin, A.M., Ed.; Kaner, N., Translator; Translation Edited by Molly Gleser; Israel Programme for Scientific Translations: Jerusalem, Israel, 1965.
10. Tsakiropoulos, P. Alloys for application at ultra-high temperatures: Nb-silicide in situ composites. Challenges, breakthroughs and opportunities. *Prog. Mater. Sci.* **2020**, *123*, 100714. [CrossRef]
11. Tsakiropoulos, P. Refractory Metal (Nb) Intermetallic Composites, High Entropy Alloys, Complex Concentrated Alloys and the alloy design methodology NICE—Mise-en-scène patterns of thought and progress. *Materials* **2021**, *14*, 989. [CrossRef] [PubMed]
12. Tsakiropoulos, P. Alloys. US Patent 10,227,680, 17 June 2009.
13. Geng, J.; Tsakiropoulos, P.; Shao, G. A thermo-gravimetric and microstructural study of the oxidation of Nb_{ss}/Nb_5Si_3 based in situ composites with Sn addition. *Intermetallics* **2007**, *15*, 270–281. [CrossRef]
14. Xu, Z.; Utton, C.; Tsakiropoulos, P. A study of the effect of 2 at.% Sn on the microstructure and isothermal oxidation at 800 and 1200 °C of Nb-24Ti-18Si based alloys with Al and/or Cr additions. *Materials* **2018**, *11*, 1826. [CrossRef]
15. Xu, Z.; Utton, C.; Tsakiropoulos, P. A study of the effect of 5 at.% Sn on the microstructure and isothermal oxidation at 800 and 1200 °C of Nb-24Ti-18Si based alloys with Al and/or Cr additions. *Materials* **2020**, *13*, 245. [CrossRef]
16. Knittel, S.; Mathieu, S.; Portebois, L.; Vilasi, M. Effect of tin addition on Nb-Si based in situ composites. Part II: Oxidation behaviour. *Intermetallics* **2014**, *47*, 43–52. [CrossRef]
17. Tsakiropoulos, P. On Nb silicide based alloys: Alloy design and selection. *Materials* **2018**, *11*, 844. [CrossRef]
18. Zelenitsas, K.; Tsakiropoulos, P. Effect of Al, Cr and Ta additions on the oxidation behaviour of Nb-Ti-Si in situ composites at 800 °C. *Mater. Sci. Eng.* **2006**, *A416*, 269–280. [CrossRef]
19. Geng, J.; Tsakiropoulos, P.; Shao, G. Oxidation of Nb-Si-Cr-Al in situ composites with Mo, Ti and Hf additions. *Mater. Sci. Eng.* **2006**, *A441*, 26–39. [CrossRef]
20. Li, Z.; Tsakiropoulos, P. On the microstructure and hardness of the Nb-24Ti-18Si-5Al-5Cr-5Ge and Nb-24Ti-18Si-5Al-5Cr-5Ge-5Hf (at.%) silicide based alloys. *Materials* **2019**, *12*, 2655. [CrossRef] [PubMed]
21. Hernandez-Negrete, O.; Tsakiropoulos, P. On the microstructure and isothermal oxidation at 800 and 1200 °C of the Nb-24Ti-18Si-5Al-5Cr-5Ge-5Sn (at.%) silicide based alloy. *Materials* **2020**, *13*, 722. [CrossRef]
22. Zhao, J.; Utton, C.; Tsakiropoulos, P. On the microstructure and properties of Nb-12Ti-18Si-6Ta-2.5W-1Hf (at.%) silicide based alloys with Ge and Sn additions. *Materials* **2020**, *13*, 1778. [CrossRef]
23. Zhao, J.; Utton, C.; Tsakiropoulos, P. On the microstructure and properties of Nb-18Si-6Mo-5Al-5Cr-2.5W-1Hf Nb-silicide based alloys with Ge, Sn and Ti additions (at.%). *Materials* **2020**, *13*, 4548. [CrossRef]
24. Okamoto, H. *Desk Handbook: Phase Diagrams for Binary Alloys*; ASM International: Materials Park, OH, USA, 2000.
25. Grammenos, I.; Tsakiropoulos, P. Study of the role of Mo and Ta additions in the microstructure of Nb-18Si-5Hf silicide based alloy. *Intermetallics* **2010**, *18*, 1524–1530. [CrossRef]
26. Grammenos, I.; Tsakiropoulos, P. Study of the role of Hf, Mo and W additions in the microstructure of Nb-20Si silicide based alloys. *Intermetallics* **2011**, *19*, 1612–1621. [CrossRef]
27. McCaughey, C.; Tsakiropoulos, P. Type of primary Nb_5Si_3 and precipitation of Nb_{ss} in αNb_5Si_3 in a Nb-8.3Ti-21.1Si-5.4Mo-4W-0.7Hf (at.%) near eutectic Nb-silicide based alloy. *Materials* **2018**, *11*, 967. [CrossRef]
28. Zacharis, E.; Utton, C.; Tsakiropoulos, P. A study of the effects of Hf and Sn on the microstructure, hardness and oxidation of Nb-18Si silicide based alloys without Ti addition. *Materials* **2018**, *11*, 2447. [CrossRef]
29. Zacharis, E. Study of the role of Hf and Sn in Nb-18Si silicide based alloys, PhD thesis, University of Sheffield, UK, 2013.
30. Bewlay, B.P.; Whiting, P.; Davis, A.W.; Briant, C.L. Creep mechanisms in niobium–silicide based in situ composites. *MRS Proc. High Temp. Ordered Intermet. Alloys VIII* **1999**, *552*, KK6.11.1–KK6.11.5. [CrossRef]

31. Bewlay, B.P.; Bishop, R.R.; Jackson, M.R. The Nb-Hf-Si ternary phase diagram: Liquid–solid phase equilibria in Nb and Hf rich alloys. *Z. Met.* **1999**, *90*, 413–422.
32. Zhao, J.-C.; Bewlay, B.P.; Jackson, M.R. Determination of Nb-Hf-Si phase equilibria. *Intermetallics* **2001**, *9*, 681–689. [CrossRef]
33. Bewlay, B.P.; Sitzman, S.D.; Brewer, L.N.; Jackson, M.R. Analyses of eutectoid phase transformations in Nb-silicide in-situ composites. *Microsc. Microanal.* **2004**, *10*, 470–480. [CrossRef] [PubMed]
34. *Triboscope User Manual*; Hysitron Ltd: Eden Prairie, MN, USA, 2005.
35. Zelenitsas, K.; Tsakiropoulos, P. Study of the role of Cr and Al additions in the microstructure of Nb-Ti-Si in situ composites. *Intermetallics* **2005**, *13*, 1079–1095. [CrossRef]
36. Zelenitsas, K.; Tsakiropoulos, P. Study of the role of Ta and Cr additions in the microstructure of Nb-Ti-Si-Al in situ composites. *Intermetallics* **2006**, *14*, 639–659. [CrossRef]
37. Vellios, N.; Tsakiropoulos, P. The role of Fe and Sn additions in the microstructure of Nb-24Ti-18Si-5Cr silicide base alloys. *Intermetallics* **2010**, *18*, 1729–1736. [CrossRef]
38. Vellios, N.; Tsakiropoulos, P. The role of Fe and Ti additions in the microstructure of Nb-18Si-5Sn silicide- based alloys. *Intermetallics* **2007**, *15*, 1529–1537. [CrossRef]
39. Vellios, N.; Tsakiropoulos, P. The role of Sn and Ti additions in the microstructure of Nb-18Si base alloys. *Intermetallics* **2007**, *15*, 1518–1528. [CrossRef]
40. Grammenos, I.; Tsakiropoulos, P. Study of the role of Al, Cr and Ti additions in the microstructure of Nb-18Si-5Hf silicide based alloys. *Intermetallics* **2010**, *18*, 242–253. [CrossRef]
41. Tsakiropoulos, P. Alloying and properties of C14-$NbCr_2$ and A15-Nb_3X (X = Al, Ge, Si, Sn) in Nb-silicide based alloys. *Materials* **2018**, *11*, 395. [CrossRef]
42. Bendersky, L.; Biancaniello, F.S.; Boettinger, W.J.; Perepezko, J.H. Microstructural characterisation of rapidly solidified Nb-Si alloys. *Mater. Sci. Eng.* **1987**, *89*, 151–159. [CrossRef]
43. Tsakiropoulos, P. Alloying and hardness of eutectics with Nb_{ss} and Nb_5Si_3 in Nb-silicide based alloys. *Materials* **2018**, *11*, 592. [CrossRef]
44. Ghadyani, M.; Utton, C.; Tsakiropoulos, P. Microstructures and isothermal oxidation of the alumina scale forming $Nb_{1.7}Si_{2.4}Ti_{2.4}Al_3Hf_{0.5}$ and $Nb_{1.3}Si_{2.4}Ti_{2.4}Al_{3.5}Hf_{0.4}$ alloys. *Materials* **2019**, *12*, 222. [CrossRef] [PubMed]
45. Bewlay, B.P.; Jackson, M.R. The Nb-Ti-Si Ternary Phase Diagram: Evaluation of Liquid-Solid Phase Equilibria in Nb- and Ti-Rich Alloys. *J. Phase Equilibria* **1997**, *18*, 264–278. [CrossRef]
46. Bewlay, B.P.; Zhao, J.-C.; Jackson, M.R.; Bishop, R.R. Determination of the effect of Hf additions on phase stability in Nb-silicide based in-situ composites. *Mater. Res. Soc. Symp. Proc.* **1999**, *552*, KK6.8.1–K6.8.6. [CrossRef]
47. Kim, W.Y.; Yeo, I.D.; Ra, T.Y.; Cho, G.S.; Kim, M.S. Effect of V addition on microstructure and mechanical property in the Nb-Si alloy system. *J. Alloys Compd.* **2004**, *364*, 186–192. [CrossRef]
48. Geng, J.; Tsakiropoulos, P.; Shao, G. The effects of Ti and Mo additions on the microstructure of Nb silicide base in situ composites. *Intermetallics* **2006**, *14*, 227–235. [CrossRef]
49. Geng, J.; Tsakiropoulos, P.; Shao, G. A Study of the Effects of Hf and Sn Additions on the Microstructure of Nb_{ss}/Nb_5Si_3 based in situ composites. *Intermetallics* **2007**, *15*, 69–76. [CrossRef]
50. Yang, Y.; Chang, Y.A.; Zhao, J.-C.; Bewlay, B.P. Thermodynamic modelling of the Nb-Hf-Si ternary system. *Intermetallics* **2003**, *11*, 407–415. [CrossRef]
51. Bewlay, B.P.; Lipsitt, H.A.; Jackson, M.R.; Reeder, W.J.; Sutliff, J.A. Solidification processing of high temperature intermetallic eutectic-based alloys. *Mater. Sci. Eng.* **1995**, *A192/193*, 534–543. [CrossRef]
52. Senkov, O.N.; Miracle, D.B.; Chaput, K.J. Development and exploration of refractory High entropy alloys—A review. *J. Mater. Res.* **2018**, *33*, 3092–3128. [CrossRef]
53. Oliver, W.C.; Pharr, G.M. An improved technique for determining hardness and elastic modulus using load and displacement sensing indentation experiments. *J. Mater. Res.* **1992**, *7*, 1564–1583. [CrossRef]
54. Papadimitriou, I.; Utton, C.; Tsakiropoulos, P. The impact of Ti and temperature on the stability of Nb_5Si_3 phases: A first-principles study. *Sci. Technol. Adv. Mater.* **2017**, *18*, 467–479. [CrossRef]
55. Kumar, K.S. *Intermetallic Compounds: Principles and Practice*; Westbrook, H., Fleischer, R.L., Eds.; John Wiley & Sons: Chichester, UK, 1995; Volume 2, p. 213.
56. Sethi, J.S. *Study of the Contamination of Nb Silicide Alloys by Interstitials*; Final Year Project; University of Sheffield: Sheffield, UK, 2012.
57. Claire, V. *Study of the Role of Refractory Metal Additions on the Hardness of Nb_{ss} and Nb_5Si_3 in Nb Silicide Based Alloys*; Final Year Project; University of Sheffield: Sheffield, UK, 2012.
58. Feng, T. *Study of the Effect of Interstitial Element Contamination on the Properties of Nb_{ss} and Nb_5Si_3 in Nb Silicide Based Alloys*; Final Year Project; University of Sheffield: Sheffield, UK, 2013.
59. Tsakiropoulos, P. On the alloying and properties of tetragonal Nb_5Si_3 in Nb-silicide based alloys. *Materials* **2018**, *11*, 69. [CrossRef]
60. Chen, Y.; Hammerschmidt, T.; Pettifor, D.G.; Shang, J.; Zhang, Y. Influence of vibrational entropy on structural stability of Nb-Si and Mo-Si systems at elevated temperatures. *Acta Mater.* **2009**, *57*, 2657–2664. [CrossRef]

61. Shi, S.; Zhu, L.; Jia, L.; Zhang, H.; Sun, Z. Ab initio study of alloying effects on structure stability and mechanical properties of Nb5Si3. *Comput. Mater. Sci.* **2015**, *108*, 121–127. [CrossRef]
62. Li, Z.; Tsakiropoulos, P. Study of the effect of Cr and Ti additions in the microstructure of Nb-18Si-5Ge based in situ composites. *Intermetallics* **2012**, *26*, 18–25. [CrossRef]
63. Li, Z.; Tsakiropoulos, P. The microstructure of Nb-18Si-5Ge-5Al and Nb-24Ti-18Si-5Ge-5Al in situ composites. *J. Alloys Compd.* **2013**, *550*, 553–560. [CrossRef]